

1 **Air-borne in-situ measurements of aerosol size distributions and**
2 **BC across the IGP during SWAAMI -RAWEX**

3 Mukunda Madhab Gogoi¹, Venugopalan Nair Jayachandran¹, Aditya Vaishya², Surendran Nair
4 Suresh Babu¹, Sreedharan Krishnakumari Satheesh^{3,4} and Krishnaswamy Krishna Moorthy³

5 ¹Space Physics Laboratory, Vikram Sarabhai Space Centre, Thiruvananthapuram – 695022, India

6 ²School of Arts and Sciences & Global Centre for Environment and Energy, Ahmedabad University,
7 Ahmedabad – 380009, India

8 ³Centre for Atmospheric and Oceanic Sciences, Indian Institute of Science, Bengaluru – 560012, India

9 ⁴Divecha Centre for Climate Change, Indian Institute of Science, Bengaluru – 560012, India

10

11

Abstract

12 During the combined South-West Asian Aerosol Monsoon Interaction – Regional Aerosol Warming
13 Experiment (SWAAMI -RAWEX), collocated air-borne measurements of aerosol number-size
14 distributions in the size (diameter) regime 0.5 to 20 μm and black carbon (BC) mass concentrations
15 were made across the Indo-Gangetic Plains (IGP), for the first time, from three distinct locations,
16 just prior to the advent of Indian Summer Monsoon over the IGP. These measurements provided an
17 east-west transect of region-specific properties of aerosols as the environment transformed from
18 mostly-arid conditions of western IGP (represented by Jodhpur, JDR) having dominance of natural
19 aerosols to the Central IGP (represented by Varanasi, VNS) having very high anthropogenic
20 emissions, to the eastern IGP (represented by the coastal station Bhubaneswar, BBR) characterized
21 by a mixture of the IGP outflow and marine aerosols. Despite these, the aerosol size distribution
22 revealed an increase in coarse mode concentration and coarse mode mass-fraction (fractional
23 contribution to the total aerosol mass) with the increase in altitude across the entire IGP, especially
24 above the well-mixed region. Consequently, both the mode radii and geometric mean radii of the
25 size distributions showed an increase with altitude. However, near the surface and within the
26 atmospheric boundary layer (ABL), the features were specific to the different sub-regions; with the
27 highest coarse mode mass fraction ($F_{\text{MC}} \sim 72\%$) in the western IGP and highest accumulation fraction
28 in the Central IGP with the eastern IGP coming in-between. The elevated coarse mode fraction is
29 attributed to mineral dust load arising from local production as well as due to advection from the
30 west. This was further corroborated by data from Cloud Aerosol Transportation System (CATS)
31 onboard International Space Station (ISS), which also revealed that the vertical extent of dust
32 aerosols reached as high as 5 km during this period. Mass concentrations of BC were moderate (~ 1
33 $\mu\text{g m}^{-3}$) with very little altitude variation up to 3.5 km, except over VNS where very high
34 concentrations were seen near the surface and within the ABL. BC induced atmospheric heating rate
35 was highest near the surface at VNS ($\sim 0.81 \text{ K day}^{-1}$), while showing an increasing pattern with
36 altitude at BBR ($\sim 0.35 \text{ K day}^{-1}$ at the ceiling altitude).

37 **Keywords:** Aerosol size distribution profile, BC mass fraction, aerosol type, IGP, monsoon.

38 **Corresponding Author:**

39 Dr. Mukunda M. Gogoi
40 Space Physics Laboratory, Vikram Sarabhai Space Centre
41 Indian Space Research Organization, Thiruvananthapuram – 695022, India
42 Email: dr_mukunda@vscc.gov.in
43 Phone: +91-471-256 3365; Fax: +91-471-270 6535
44

45 **1. Introduction**

46 The Indo-Gangetic Plains (IGP) remains one of the global hotspots of aerosols. The prevailing high
47 aerosol loading and the relative abundance of its constituents (being a mixture of natural and
48 anthropogenic species) is known to show significant seasonality (Gautam et al., 2011; Praveen et
49 al., 2012; Moorthy et al., 2016; Vaishya et al., 2018; Rana et al., 2019; Brooks et al., 2019). This
50 arises due to combined effects of the dense population and the associated anthropogenic and
51 industrial activities, as well as the loose alluvial soil of this regions having vast semi-arid and arid
52 characteristics to the west. A dense network of thermal power-plants, several of them being coal
53 fired, is among the prominent source of anthropogenic emissions over the region. This is abetted by
54 the synoptic meteorology with its strong seasonality (Gautam et al., 2010; Nath et al., 2018; Singh
55 et al., 2018) and the orography that slopes down from the west to east bound on the north and south
56 respectively by the Himalayas and the Aravalli ranges and Bihar Plateau forming a confined channel
57 (Moorthy et al. 2007; Gogoi et al., 2017). For accurate quantification of the radiative implications
58 of this complex aerosol system, several concerted studies have been made using ground based (Giles
59 et al., 2012; Bansal et al., 2019) and space-borne measurements (Srivastava, 2016; Mhawish et al.,
60 2017; Kumar et al., 2018) as well as numerical modeling (Govardhan et al., 2019). However, most
61 of these studies have uncertainties arising out of the ill-represented altitude variation of aerosol
62 properties due to sparse measurements. Height resolved in-situ measurements of aerosol properties
63 are indispensable not only in this regard, but also for understanding aerosol-cloud interactions.

64 In recent years, a few campaign-mode airborne measurements have been made over this region to
65 estimate the altitude-resolved properties of aerosols that are important in aerosol-radiation
66 interactions (Padmakumari et al., 2013; Babu et al., 2016; Nair et al., 2016; Vaishya et al., 2018;
67 Gogoi et al., 2019). These include the measurements of aerosol scattering and absorption coefficients
68 conducted as part of the Regional Aerosol Warming Experiment (RAWEX; Babu et al., 2016) to
69 delineate the spatio-temporal variability in the altitude distribution of aerosol single scattering albedo
70 (SSA) across the IGP during winter and pre-monsoon seasons and aerosol and cloud parameter
71 measurements conducted as part of the Cloud Aerosol Interaction and Precipitation Enhancement
72 Experiment (CAIPEEX; Kulkarni et al., 2012). Some studies have also reported significant
73 contribution of dust and BC to the elevated aerosol load (Praveen et al., 2012; Kedia et al., 2014;
74 Pandey et al., 2016; Li et al., 2016) and their potential role to act as ice nuclei (Padmakumari et al.,
75 2013). However, despite its importance in radiative interactions and CCN activation, the altitude-
76 resolved measurements of aerosol size distribution are extremely sparse, or non-existent, especially
77 just prior to the onset of the Indian Summer Monsoon, when the sources of aerosols, their mixing

78 and transport pathways are all complex. The information on aerosol size distribution is important for
79 accurately describing the phase function, which describes the angular variation of the scattered
80 intensity. The knowledge of its vertical variation would thus improve the accuracy of ARF
81 estimation and hence heating rates. Such information is virtually non-existing over this region.
82 Further, the knowledge of the variation of size distribution with altitude would be useful in better
83 understanding the aerosol-cloud interactions and CCN characteristics, during the evolving and active
84 phase of the Indian monsoon. This was among the important information aimed to be obtained under
85 SWAAMI - RAWEX (<https://gtr.ukri.org/projects?ref=NE%2FL013886%2F1> and
86 <http://www.spl.gov.in/SPL/index.php/arfs-research/field-campaigns/asfasf>) - a joint Indo-UK field
87 experiment involving airborne measurements using Indian and UK aircrafts during different phases
88 of the Indian monsoon, right from just prior to the onset of monsoon (i.e. in the beginning of June).

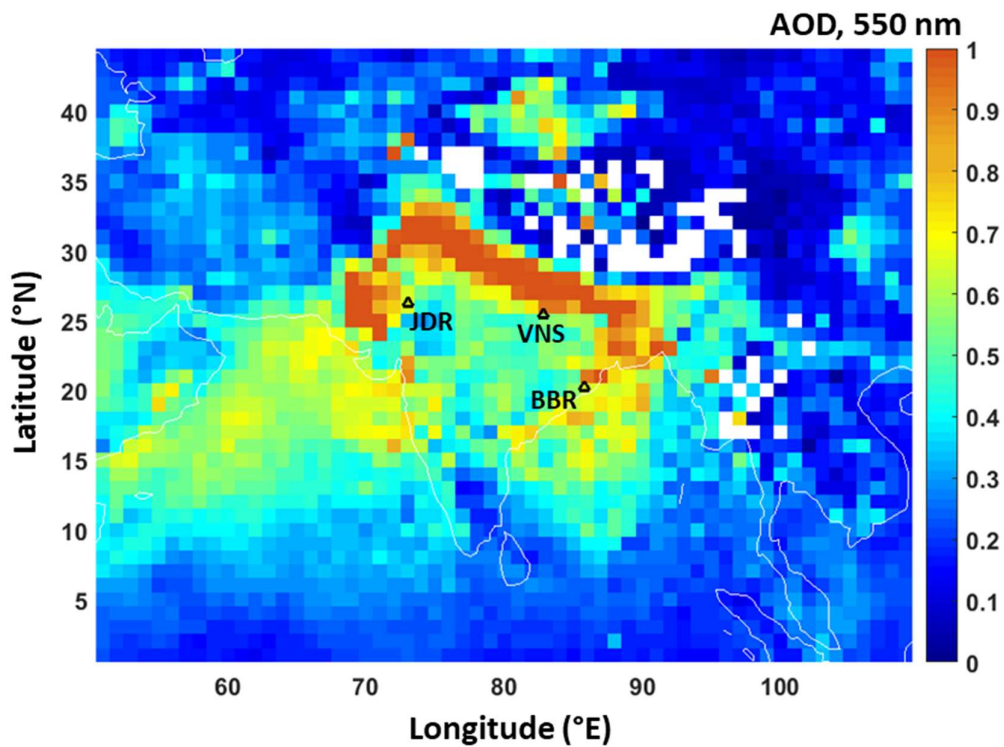
89 During this campaign, vertical profiles of various aerosol parameters have been measured using an
90 instrumented aircraft from three base stations –representing western, central and eastern end of the
91 IGP– during 01 to 20 June 2016, just prior to onset of the Indian summer monsoon. Some important
92 results on the optical and CCN characteristics are already reported (Vaishya et al., 2018;
93 Jayachandran et al 2020). In the present study, we have examined the vertical profiles of aerosol
94 number-size distributions in the size (diameter) regime 0.5 to 20 μm and black carbon (BC) mass
95 concentrations. The results are presented and discussed in the light of other supplementary
96 information.

97 **2. Experimental Details and database**

98 **2.1 Study region and flight details**

99 The base stations (Figure-1), from where the aircraft operations were carried out, represented distinct
100 regions of the IGP; ‘Jodhpur (JDR; 26.25°N, 73.04°E)’ in the western IGP is an arid/ semi-arid
101 region with low urban activities, lying downwind the ‘Great Indian Desert’ to its west (JDR has
102 population density of 161 per sq. km). ‘Varanasi (VNS; 25.44°N, 82.85°E)’ in the central IGP is
103 located downwind of Jodhpur, characterized by extensive anthropogenic activities (automobiles,
104 small and large-scale industries and thermal power plants and wide spread agricultural activities) by
105 its dense population (density 2,399 km^{-2}). ‘Bhubaneswar (BBR; 20.25°N, 85.81°E)’ is an urban
106 location in the eastern IGP (population density of 2131 km^{-2}), and experiences the influence of
107 marine aerosol component from the Bay-of-Bengal (~ 50 km away from the base station) in addition
108 to the influence of IGP outflow and local aerosol sources from nearby thermal (coal based) power
109 plants, mining and fertilizer based industries etc. (Panda et al., 2016). The northwestern part of India

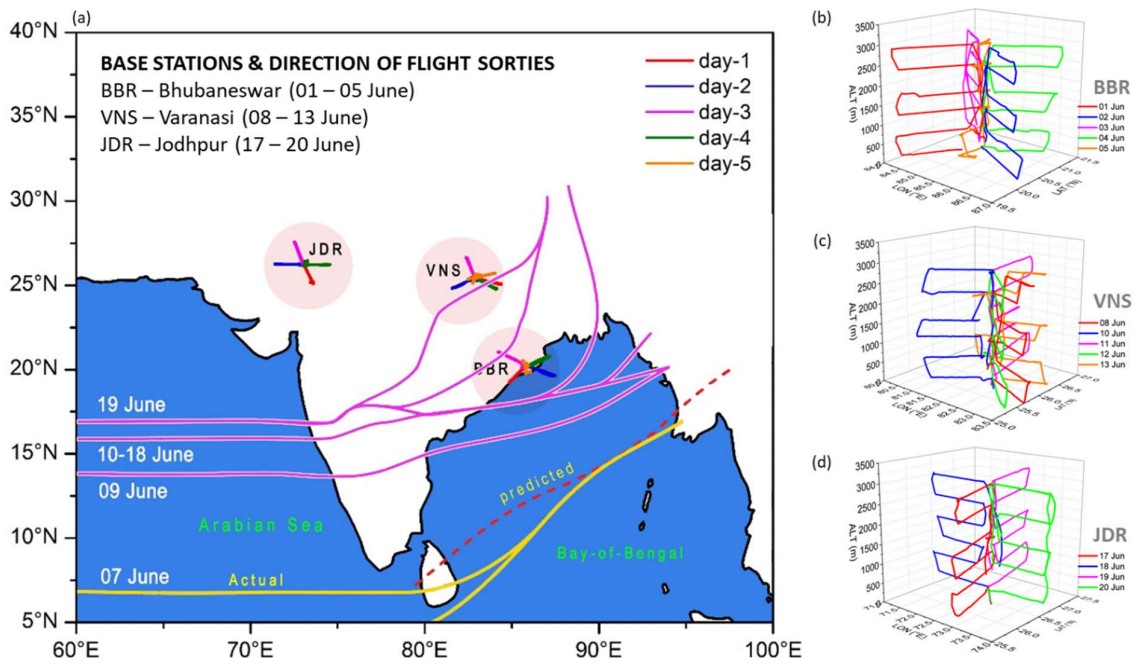
110 has an undulating topography, due to which monsoon currents loose moisture while crossing the
111 western mountain ranges (Aravalli) and results in dry arid regions (Moorthy et al., 2007). Strong
112 dust-rising winds are a common feature of the IGP in general and its western parts in particular
113 during April to July (Banerjee et al. 2019). In the central IGP, VNS and its environs hold largely
114 even topography, where the Ganga is the principal river. In the eastern IGP, BBR is topographically
115 decorated with western uplands and eastern lowlands, with hillocks in the western and northern parts.
116 These base stations, thus provided a west-east cross section of the highly aerosol laden IGP; where
117 the aerosol characteristics are known to change longitudinally. The spatial map of AOD at 550 nm
118 (Figure-1) clearly shows the existence of higher aerosol loading ($AOD > 0.5$) over the observational
119 site during the study period.



120

121 **Figure-1:** Three distinct base stations: (i) ‘Jodhpur (JDR; 26.25°N, 73.04°E)’ in the western IGP,
122 (ii) ‘Varanasi (VNS; 25.44°N, 82.85°E)’ in the central IGP and (iii) ‘Bhubaneswar (BBR; 20.25°N,
123 85.81°E)’ in the eastern coastal IGP, from where the aircraft measurements were conducted. The
124 spatial map of AOD at 550 nm obtained from MODIS sensor (MOD08_D3_6.1, Dark-Target and
125 Deep-Blue combined mean) on-board Terra satellite during the study period (01-20 June 2016) is
126 shown in the background.

127 Figure-2a shows the actual dates of onset of the monsoon at different parts of India in 2016. As can
 128 be seen from the figure, despite a delayed onset at the southern tip of India, monsoon advanced fast
 129 in to the central/northern parts of India. Yet, all the flight sorties from the respective base stations
 130 were completed ahead of the advent of monsoon to that station. At the eastern IGP, the aircraft sorties
 131 were made from 'BBR' before the onset of monsoon over India; at 'VNS', the flights were conducted
 132 while monsoon advanced only to the central peninsula. The final set of sorties were conducted at
 133 'JDR' when the monsoon covered most of the central and eastern part of India, but yet to progress
 134 towards northwestern parts.



135

136 **Figure-2:** (a) The onset (actual) of SW-Monsoon at different parts of India, shown by the yellow
 137 and pink (solid) lines. Horizontal and vertical flight paths during each of the sorties at (b)
 138 Bhubaneswar (BBR), (c) Varanasi (VNS) and (d) Jodhpur (JDR).

139 From each of the base stations, 4 to 5 sorties were carried out on successive days in different
 140 horizontal directions about the station, as shown by the ground projections (horizontal lines in Fig
 141 2a), with a view to obtain an average sub-regional representation in the shortest time possible. During
 142 each of the sorties, measurements were made at six discrete levels following a staircase configuration
 143 as shown in Figure 2 b-d (for JDR, VNS and BBR respectively). Accordingly, the aircraft initially
 144 climbed to the base/ceiling altitude, stabilized and made horizontal flight along the projected track
 145 for about 30 min before climbing up/ down to the next higher/ lower levels and stabilizing. This

146 procedure was repeated for all levels (~ 0.5, 1, 1.5, 2, 2.5 and 3 km a.g.l.) until the last level. The
147 ceiling altitude was restricted to 3.5 km based on the unpressurised mode of operation of the aircraft.
148 All the flights were carried out around mid-day since thorough vertical mixing is established by the
149 daytime convective boundary layer eddies.

150 2.2. On-board Instrumentation

151 The measurements were carried out aboard the instrumented aircraft (Beechcraft-200) fitted with an
152 iso-kinetic inlet, mounted (front facing) at the bottom of the fuselage for aspirating ambient aerosols
153 and detailed in earlier papers (Babu et al., 2016; Vaishya et al., 2018; Gogoi et al., 2019). A constant
154 volumetric flow of 70 LPM was maintained using an external pump connected to the main inlet
155 assembly, which provided iso-kinetic flow for the average speed of 300 km/hr maintained by the
156 aircraft during the entire campaign. The efficiency of this inlet system has been already proven in
157 several previous campaigns (Babu et al., 2016; Nair et al., 2016; Gogoi et al., 2019).

158 *Measurement of aerosol size distribution*

159 A factory-calibrated, Aerodynamic Particle Sizer (APS) spectrometer (TSI, Model: 3321) is used
160 for the measurement of aerosol size distribution. It measures size-resolved number concentration of
161 the ambient aerosols in the size range from 0.5 to 20 μm , over 52 channels spaced equally in
162 logarithmic size bins; at a sampling frequency of 1-minute. Aerosol particles in this size range is
163 most important in influencing the optical (scattering and extinction) and CCN and ice nuclei (IN)
164 characteristics.

165 The APS measures the concentration of particles in terms of their aerodynamic diameters by
166 comparing the velocity of particle (controlled by an accelerating flow field) to that of a unit density
167 sphere having same velocity. Particle velocity is estimated from the measurement of time of flight
168 (Mitchell and Nagel, 1999). In the present study a sheath flow at 4 LPM (litres per minute) was
169 maintained against the sample flow of 1 LPM. The instrument automatically adjusts the flow rates
170 with changes in ambient pressure to maintain the specified flow rates. Occasionally, when the
171 aircraft passes through clouds, the aerosol number concentration shot up from the otherwise stable
172 values. Such outliers are removed following 2σ criteria, wherein data points at a particular level
173 lying outside 2σ values of the level-average were removed. The number of such screened out points
174 were $< 3\%$ of the total. The consistency in the flow was periodically checked each time, before start
175 of measurements from the new base station. Similarly, the optical components and tubing of the
176 system were cleaned immediately after moving to a new base station.

177 The TSI-APS (3321) is suitable for operating at 10 to 90% RH (non-condensing) and 10 - 40 °C
178 ambient temperature. For BBR, it is likely that aerosols grew under high RH conditions but might
179 have also shrunk due to higher instrument temperature as compared to ambient. However, more
180 controlled laboratory experiments are required to ascertain the response of the APS to hygroscopic
181 growth of particles.

182

183 *Measurement of Black Carbon aerosols*

184 Mass concentration of ambient BC aerosols was estimated using a 7-channel aethalometer (Model:
185 AE-33, Magee Scientific, USA), which measures the attenuation of light that passes through the
186 aerosol laden filter at wavelengths 370, 470, 520, 590, 660, 880, and 950 nm. The loading (or
187 shadowing) effect arising out of the successive deposition of aerosols in the filter media is
188 automatically compensated in real-time in the new-generation Aethalometer; while the multiple
189 scattering effects were minimised by using advanced filter tape material (Drinovec et al.,2015). In
190 the present study, BC mass concentrations were obtained at 1-minute interval by operating the
191 aethalometer at 50% of the maximum attenuation, and a standard mass flow rate of 2 LPM under
192 standard temperature (T_0 , 293 K) and pressure (P_0 , 1013 hPa). As the unpressurised aircraft climbed
193 higher, the instrument experienced ambient pressure (P) and temperature (T). In order to maintain
194 the set mass flow, the pumping speed of the instrument was automatically increased (through internal
195 program) to aspire more volume of air. However, the volume of air aspirated at ambient pressure
196 and temperature requires to be corrected to standard atmospheric condition for the actual estimate
197 of BC (Moorthy et al., 2004). Thus, the actual volume of air aspirated by the Aethalometer at
198 different atmospheric level is,

$$199 \quad V = V_0 \frac{P_0 T}{P T_0}$$

200 Thus, true BC mass concentration (M_{BC}) is

$$201 \quad M_{BC} = M_{BC}^* \left[\frac{P_0 T}{P T_0} \right]^{-1} \quad (1)$$

202 Here, M_{BC}^* is the instrument measured raw mass concentration of BC at ambient pressure and
203 temperature. Details of the aethalometer principle, operation, uncertainty involved and error budget
204 are reported in several earlier literatures (Weingartner et al., 2003; Arnott et al., 2005; Gogoi et al.,
205 2017). In general, the instrumental uncertainty ranges from 50% at 0.05 $\mu\text{g m}^{-3}$ to 6% at 1 $\mu\text{g m}^{-3}$

206 (Corrigan et al., 2006) and the uncertainty in the estimation of absorption coefficients is around 10%
207 (Vaishya et al., 2018).

208 2.4. General synoptic meteorology during the campaign

209 The meteorological conditions across the IGP during the campaign period was generally hot (surface
210 temperature, $T \sim 34.7 \pm 2.8$ °C at JDR, 39 ± 1.9 °C at VNS and 32.8 ± 3.6 °C at BBR at the time of
211 flight take off), with low to moderate relative humidity (RH) at JDR(RH $\sim 40\%$) and VNS (RH \sim
212 60%). The values of RH at BBR was relatively higher (as high as 80%) associated with its coastal
213 proximity, in addition to the influence of mild pre-monsoon rainfall during the first (01-June-2016;
214 light rain during noon), third (03-June-2016; heavy rain ~ 60 mm in the night) and fourth (04-June-
215 2016; light rain in the morning and during noon) days of observations. The records of T and RH
216 were obtained from the sensors on-board the aircraft, while the rainfall data was obtained from the
217 airport meteorological department at BBR.

218 2.3. Supplementary data

219 Supplementary data used in this study include aerosol backscattering coefficients and depolarization
220 ratio measured by the *Cloud Aerosol Transportation System* (CATS) aboard the International Space
221 Station (ISS). The CATS is a comprises of an elastic backscatter lidar consisting of two high
222 repetition rate (4-5 kHz), low energy (1-2 mJ) Nd:YVO₄ lasers operating at three wavelengths (1064,
223 532, and 355 nm). The receiver subsystem consists of a 60 cm telescope having a 110 micro-radian
224 field of view, photon-counting detectors, and associated control electronics (Yorks et al., 2014;
225 2016). As the altitude of ISS orbit is about 405 km (51-degree inclination), CATS provides a
226 comprehensive coverage of the tropics and mid-latitudes, with nearly a three-day repeat cycle. Level
227 2 data of CATS (<https://cats.gsfc.nasa.gov/data/>) are used (Lee et al., 2018) in the present study,
228 which provides the geophysical parameters, such as the vertical feature mask, profiles of cloud and
229 aerosol properties (i.e. extinction, particle backscatter), and layer-integrated parameters (i.e. lidar
230 ratio, optical depth). In addition, types of aerosols are also derived based on CATS typing algorithms
231 where eight aerosol types (in CATS mode 7.1) are identified: volcanic, dust, dust mixture,
232 clean/background, polluted marine, marine, polluted continental and smoke. Incorporating the
233 information of backscatter color ratio (1064/532-nm) and spectral depolarization (ratio of
234 perpendicular to parallel backscatter) ratio(1064/532-nm), Mode 7.1 provides the characteristic of
235 aerosol regimes (York et al., 2016) as below:

236

237 **Table-1:** Classification of aerosol types for CATS mode 7.1 (York et al., 2016).

Aerosol Type	Aerosol feature base	Depolarization ratio (δ'_{1064})	Color Ratio (γ'_{1064})
Volcanic	> 10 km	-	-
Dust	< 10 km	> 0.3	-
Dust mixture	< 10 km	$0.2 > \delta > 0.3$	-
Clean/background	< 10 km	-	$< 0.0005 \text{ sr}^{-1}$
Polluted marine	< 10 km	$\delta'_{1064}/\delta'_{532} > 50\%$	$\gamma'_{532}/\gamma'_{1064} < 1.75$
Marine	< 10 km	$\delta'_{1064}/\delta'_{532} < 50\%$	$\gamma'_{532}/\gamma'_{1064} < 1.75$
Polluted continental	< 10 km	$\delta'_{1064}/\delta'_{532} > 50\%$	$\gamma'_{532}/\gamma'_{1064} > 1.75$
Smoke	< 10 km	$\delta'_{1064}/\delta'_{532} < 50\%$	$\gamma'_{532}/\gamma'_{1064} > 1.75$

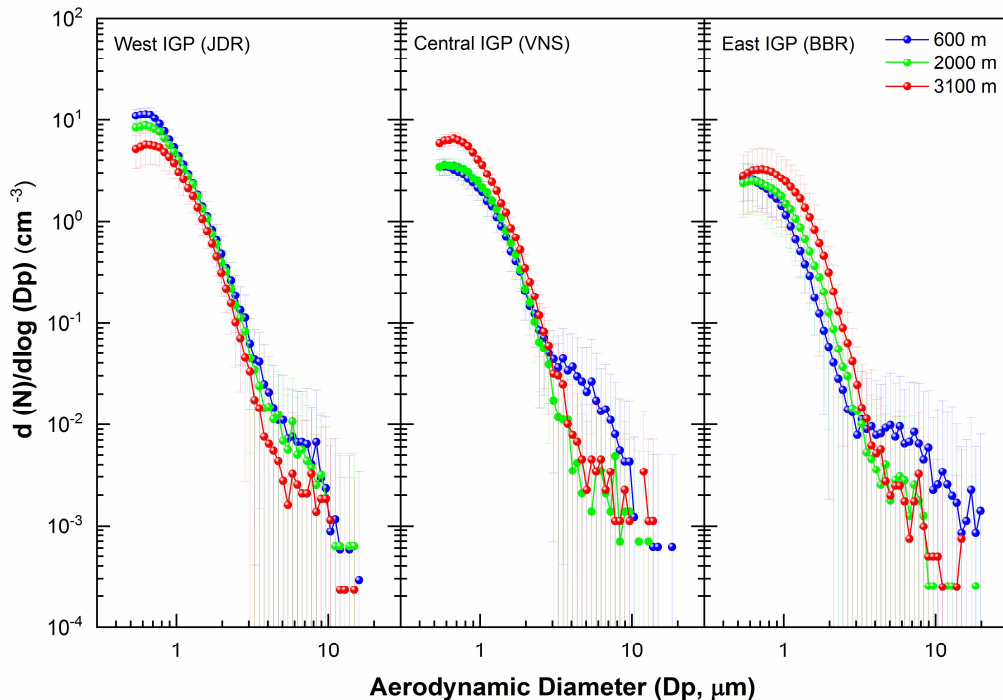
238

239

240 3. Results and discussion

241 3.1 Aerosol number size distributions

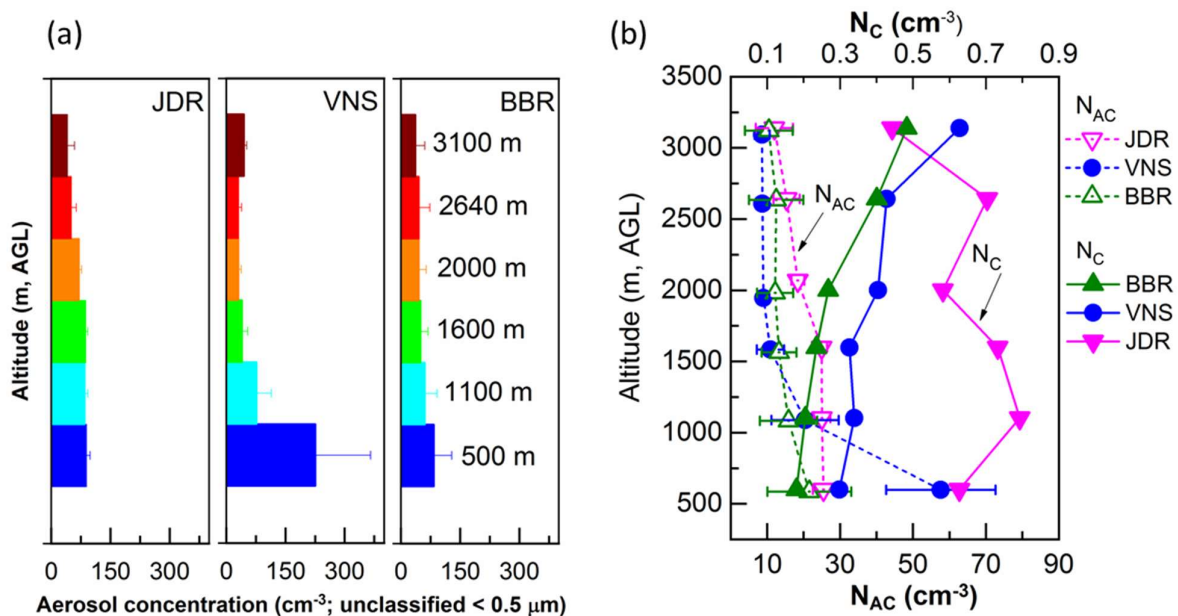
242 Aerosol number size distributions [$dN/d(\log D_p)$], representative of each of the 3 sub-regions of
 243 IGP, are presented in Figure 3; the panels from left to right representing the sub-regions JDR, VNS
 244 and BBR, from the west to east IGP.



245

246 **Figure-3:** Aerosol number size distributions (mean profiles averaged for all the days) at three
 247 distinct altitudes of JDR, VNS and BBR, representative of (i) near the surface (600 m above ground
 248 level) having proximity to emission sources, (ii) in the upper ABL (2000 m above ground level) and
 249 (iii) in the free troposphere (3100 m). Vertical bars over the points are the ensemble standard
 250 deviations. Individual size distributions at different heights of ~ 500 m interval are given in
 251 supplementary figure-S1.

252 Three distributions are shown for each station, representative of (i) near the surface with proximity
 253 to emission sources (600 m AGL), (ii) in the upper ABL (2000 m AGL) and (iii) in the free
 254 troposphere (3100 m AGL) following the mean ABL heights (1.3 ± 0.5 km, 2.3 ± 0.5 km and $1.4 \pm$
 255 0.2 km for JDR, VNS, and BBR respectively; Vaishya et al., 2018) at local noon time. Aerosol
 256 number concentration below $0.542 \mu\text{m}$ are not size-classified and represented as a single count
 257 (between 0.3 and $0.542 \mu\text{m}$) are shown as a function of altitude in Figure 4 (a).



258
 259 **Figure-4:** Vertical profiles of aerosol number concentrations;(a) between 0.3 and $0.54 \mu\text{m}$ (in the
 260 unclassified size range of APS); (b) in the accumulation and coarse mode size range (between 0.3
 261 and $20 \mu\text{m}$, denoted by N_{AC}) along with coarse mode number concentrations (N_C).

262 The figures clearly reveal that at all altitudes above different stations, the size distributions are
 263 consistently bimodal, with a prominent accumulation mode ($<1 \mu\text{m}$) and a weaker secondary mode
 264 ($>1 \mu\text{m}$). The concentration of particles in the unclassified size regime (below $0.542 \mu\text{m}$), showed a
 265 gradual decrease with increase in altitude at all stations and a spatial distinctiveness with highest

266 near surface concentration in the Central IGP (most anthropogenically impacted sub-region of the
267 IGP) depicting sharper altitude variation as against the other two sub-regions.

268 As it is well-established that during pre-monsoon/ prior to the onset of monsoon, both the natural
269 and anthropogenic aerosol species coexist in large abundance over the IGP, we examined in Figure
270 4b, the altitude profiles of accumulation mode aerosols (concentration below 1 μm), which are
271 mostly attributed to be of anthropogenic origin and coarse mode aerosols (above 1 μm), which are
272 mostly of natural origin. Accumulation mode aerosol concentration showed only weak altitudinal
273 dependence above 1 km at all the sub-regions, though at VNS, there was a sharp increase in the
274 concentration below 1 km, obviously due to source-proximity. This feature is seen in Figure 4a also.
275 This observation is supported by the collocated measurements of aerosol total number concentrations
276 (N_T) as measured by a condensation nuclei (CN) counter aboard the aircraft (Jayachandran et al.,
277 2020) in the size range above 2.5 nm, showing highest values of N_T in the entire altitude range of
278 measurements over VNS. On the other hand, the vertical profiles of coarse mode aerosol
279 concentrations (N_C) showed significantly large abundance over the western IGP (arid/ semi-arid
280 regions) represented by JDR, similar to the spring time observations reported by Gogoi et al., (2019).

281 These observations are also in-line with the reported values of dust fractions (Vaishya et al., 2018)
282 during the same campaign, showing the enhancement of dust fraction from 10 to 20 % at 300 m to
283 more than 90 % above 2 km altitude at JDR; while smallest dust fraction (< 10%) was observed at
284 BBR in the entire altitude range. Over the central IGP, synoptic wind-driven desert dust aerosols,
285 leads to elevated layers of aerosols having higher dust fraction (>50%). However, it should be noted
286 that dust over the central IGP is more absorbing in nature because of its mixing with other
287 anthropogenic emissions (such as BC; Vaishya et al., 2018), while that over western IGP is rather
288 pristine in nature. Thus, quantification of the absolute magnitude of coarse mode aerosol
289 concentrations is very important to understand the significance of elevated aerosol load on radiative
290 perturbations.

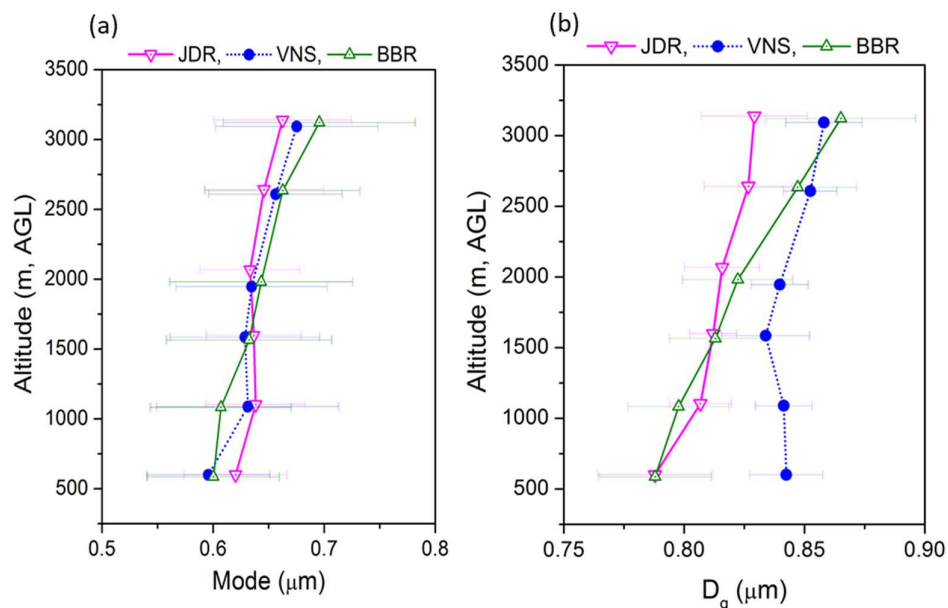
291 The increasing concentration of coarse mode particles with the increase in altitude across the entire
292 IGP is another interesting feature in the present study; which is most conspicuous at the central IGP
293 and least at the west, implying their increasing role at higher altitude; probably due to the lofted
294 regional dust and advected mineral dust from west Asian regions.

295 With a view to quantifying this, the size distribution spectra are averaged for each altitude level and
296 for each station. From these spectra, the geometrical mean diameter (D_g) is estimated as a function
297 of altitude, using the following equation

$$298 \quad D_g = \exp \left[\frac{\sum_i^n n_i \ln(D_{pi})}{N} \right] \quad (2)$$

299 where $D_{pi} (= \sqrt{D_i * D_{i+1}})$ denotes the geometric midpoint of each channel of the APS, n_i is the
300 particle concentration in i^{th} channel and $N = \sum_i^n n_i$ is the total concentration. Accordingly, D_g of a
301 spectrum of particles is the 50% probability point of an equivalent diameter having half of the
302 particle concentrations larger than this size and remaining half is below that. The vertical profiles of
303 D_g and mode ($= D_p(n_{max})$) of the distributions are shown in Figure 5. It clearly shows the increase
304 of the coarse mode fraction in the size distribution; with both the mode and D_g showing a steady
305 increase with altitude; especially D_g . The rate of increase of D_g with altitude increases from west to
306 east across the IGP, with highest values at BBR (Figure 5b). In the central IGP where mixed aerosol
307 type prevails, the increase in D_g within the ABL is rather weak, but in the free troposphere it
308 increases more sharply probably due to the faster decrease in the accumulation mode concentration
309 (Figure 4) or the prevalence of advected dust at higher altitudes or both.

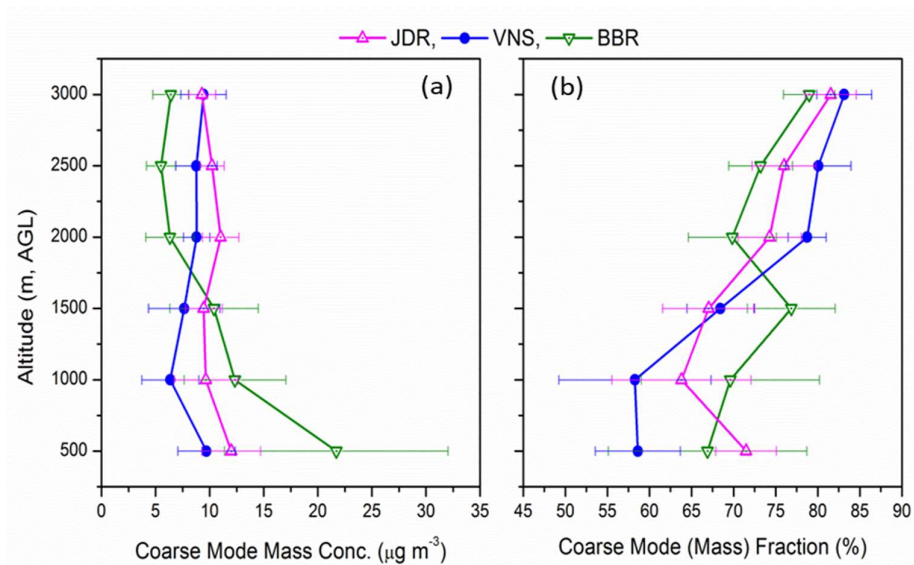
310 The observations that have foregone reveal the non-uniform distribution of dust and anthropogenic
311 sources of aerosols. Nearly steady values of N_c in the entire column at JDR are attributed to the
312 strong convective mixing of coarse mode dust aerosols up to the lower free tropospheric region. On
313 the other hand, altitude variation of accumulation and coarse mode aerosols are relatively more
314 fluctuating at BBR and VNS, compared to that at JDR (Figure 4b) as indicated by the profiles of D_g .



315

316 **Figure-5:** Vertical profiles of (a) mode and (b) geometric mean diameters (D_g) of aerosol number
 317 size distributions at different heights above the ground level, indicating the change in the pattern of
 318 distribution with altitude and from the western to the eastern part of the IGP.

319 Apart from the number-weighted expression of aerosol size distributions, the mass-weighted
 320 distributions carry useful information for quantifying regional distinctiveness of the dominance of
 321 coarse mode particles. Even though the fine mode aerosols are extremely numerous in the
 322 atmosphere and important for microphysical processes, they represent only a very small proportion
 323 of total particle mass; whereas coarse mode particles, even though far less numerous, have
 324 significant mass/ volume. In simple terms, particle number concentrations are dominant in the fine
 325 mode ($< 0.1 \mu\text{m}$), the surface area is predominantly in the accumulation mode (0.1 to $1 \mu\text{m}$), and the
 326 volume, and hence mass, is divided between the accumulation mode and coarse particle mode. In
 327 the present study, since the size range of particle counts are confined in the accumulation and coarse
 328 mode regimes (between the 0.5 and $20 \mu\text{m}$), quantitative picture of aerosol mass concentrations is
 329 obtained by assuming a uniform density equal to 2 g cm^{-3} following Moorthy et al., (1998) and Pillai
 330 et al., (2001). Since the size-resolved particle densities are not known, we did not use effective
 331 density (mass-mobility relationship defined as the mass of the particle divided by its mobility
 332 equivalent volume) of particles to calculate the mean particle mass size distributions.



333

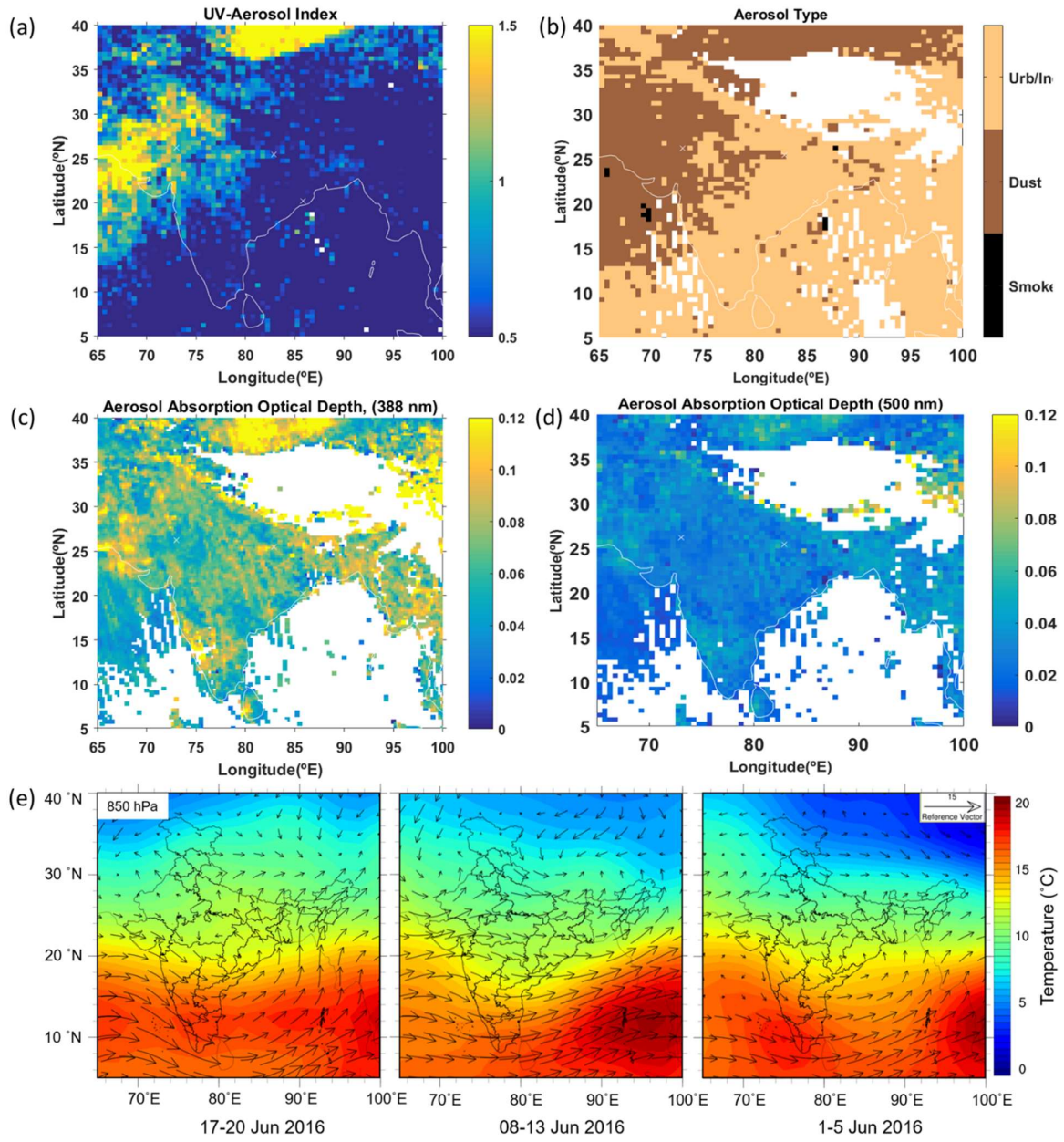
334 **Figure-6: (a)** Vertical profiles (mean and standard deviations) of coarse mode aerosol mass
 335 concentrations (M_C). The values are derived from the aerosol number concentrations at different size
 336 bins, assuming a density of 2 gm/cm^3 ; (b) Vertical profiles of aerosol coarse mode fractions (F_{MC}) at
 337 different locations.

338 Figure 6a shows the altitudinal variation of coarse mode aerosol mass concentrations over all the
 339 observational sites, along with the values of coarse mode mass fractions (F_{MC}). Over VNS and JDR,
 340 consistently higher values of M_C were seen in the entire altitude range. This is in line with the higher
 341 values of coarse mode aerosol concentrations (N_C) at these sites, JDR being the highest. On the other
 342 hand, the values of M_C at BBR decreased significantly from the surface to lower free-tropospheric
 343 region. The higher values M_C observed near the surface at BBR can be attributed to the influence of
 344 local sea-salt aerosols; however not affecting the values of D_g , due to the abundance of accumulation
 345 mode aerosols over this site.

346 Similar to that of N_C , F_{MC} showed (Figure-6b) gradually increasing values with altitude at all the
 347 locations. The high values of coarse mode mass fraction and an increasing trend with altitude is
 348 indicative of the role of upper level transport of dust from the western desert regions, in addition to
 349 those contributed locally due to thermal convective processes. As compared to other two stations,
 350 highest value of F_{MC} ($\sim 70\%$) near the surface was seen at JDR indicating the role of arid nature of
 351 the region. This exercise clearly explains the abundance coarse mode dust decreasing from west to
 352 east; along with an increase in the contribution of anthropogenic fine/ accumulation mode aerosols.

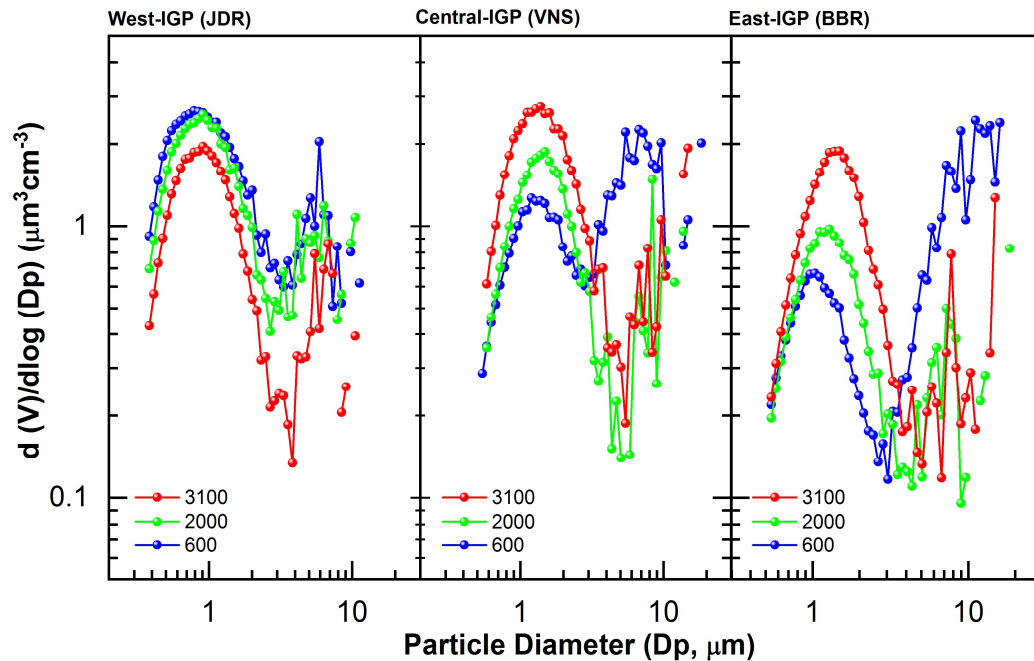
353 With a view to examine the transport of mineral dust (by the synoptic winds), the spatial distributions
354 of UV-aerosol index, aerosol types and aerosol absorption optical depth (AAOD); all derived from
355 the Level-3 OMAERUVd data product (daily, 1.0 degree x 1.0 degree) from Ozone Monitoring
356 Instrument (OMI, on-board Aura satellite; Levelt et al., 2006), are examined. OMAERUV uses the
357 pixel level Level-2 Aerosol data product of OMI at three wavelengths (355 nm, 388 nm and 500 nm)
358 to derive AAOD. Higher values of AAOD at 388 nm are indicative of the presence of dust or biomass
359 burning aerosols. This is because absorption by dust and organic carbon from biomass burning
360 sources have strong wavelength dependency, with higher absorption at near-UV wavelengths. As
361 the period of this campaign was devoid of major fire activities over the study region (northern India)
362 which normally peaks in April to May and October to November, corresponding to burning after the
363 wheat and rice harvests (Vadrevu et al., 2011; Venkataraman et al., 2006), the AAOD values would
364 be representative of dust loading. This aspect is conformed in the subsequent section using lidar
365 depolarization ratio.

366 Figure 7a-d shows the spatial distributions of UV aerosol index, aerosol type and AAOD at 388 nm
367 and 500 nm, while the synoptic winds are shown in Figure 7e. A very good association between the
368 westerly advection and dust loading extending from west to central IGP is noticeable from the figure.
369 This lends further support to the role of advected dust leading to higher M_C and F_{MC} at higher
370 altitudes, seen in figures 6. In this context, it is also worth noticing that based on observational data
371 and regional climate modeling, Banerjee et al., (2019) have clearly shown (in their Figure 7) the
372 significant vertical extent of dust loading, both of local and remote origin, during pre-monsoon and
373 summer across the IGP reaching altitudes as high as 600 hPa.



374

375 **Figure-7:** Spatial distribution of (a) UV aerosol index, (b) aerosol type, (c) aerosol absorption optical
 376 depth (AAOD) at 388 nm and (d) AAOD at 500 nm during June 2016. (e) Synoptic wind and
 377 temperature at 850 hPa.



378

379 **Figure-8:** Aerosol volume size distributions (mean profiles averaged for all the days) at three distinct
 380 altitudes (600 m, 2000 m and 3000 m) of the atmosphere (shown by different color) over JDR, VNS
 381 and BBR.

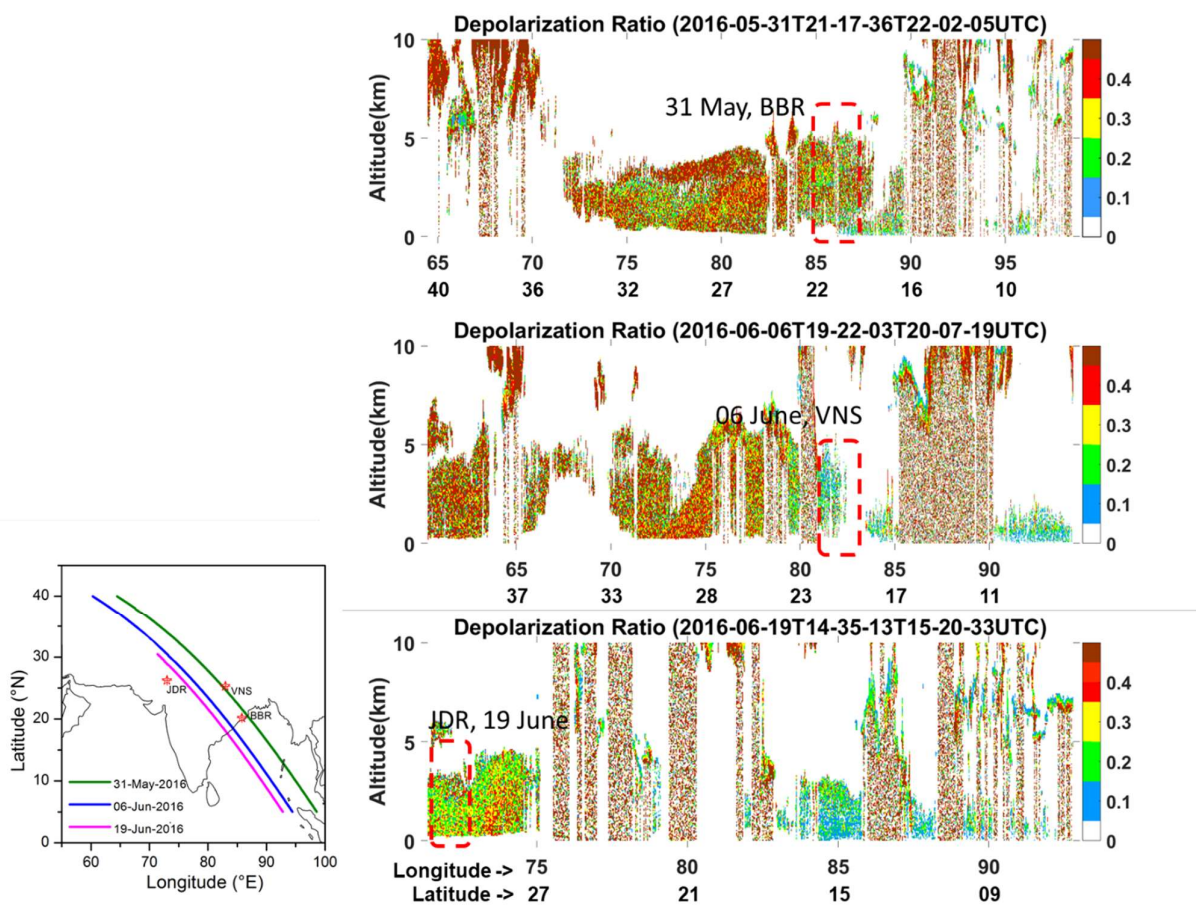
382 The volume size distribution of aerosols (shown in Figure 8) at three distinct altitude regions of the
 383 atmosphere also clearly shows the altitudinal change in the pattern of distribution, changing from
 384 coarse mode dominance near the surface to accumulation mode dominance at the ceiling altitude
 385 over BBR. While those at JDR, the pattern of distributions remains same in the entire column.
 386 Similar to JDR, VNS also depicted significant enhancement in coarse mode aerosols in the upper
 387 levels (at 2 and 3 km altitudes) of the atmosphere. Similar to these observations, based on the
 388 collocated spectral scattering properties of aerosols obtained during the same experiment, Vaishya
 389 et al., (2018) have reported that, the aerosol population changes from super-micron mode dominant
 390 natural aerosols to sub-micron mode dominant anthropogenic aerosols, as we move from west to
 391 east in the IGP. Moreover, the large abundance of coarse particles ($>2\mu\text{m}$) along with significant
 392 fine/ accumulation mode aerosols in the column highlights the complex mixture of dust with other
 393 anthropogenic components in all the three regions, making a complex scenario for aerosol radiation
 394 and aerosol cloud interaction processes. Based on the combination of satellite remote sensing and
 395 regional climate model simulations, Banerjee et al., (2019) have also shown the presence of dry
 396 elevated layer of dust (at altitudes between 850 and 700 hPa; taking place in multiple layers) during

397 June across the IGP, transported from the Thar Desert to the northern Bay-of-Bengal. To ascertain
 398 this further, we have examined the data from CATS aboard ISS.

399 3.2 Inferences from the CATS data

400 Geophysical parameters derived from the CATS on-board ISS are very useful to infer on aerosol
 401 features in the atmospheric column, especially at altitudes above the ceiling altitude of the aircraft
 402 (3.1 km). In the present study, we have considered three products from CATS for the campaign
 403 period, viz. (i) depolarization ratio, (ii) attenuated backscatter coefficients and (iii) aerosol types.

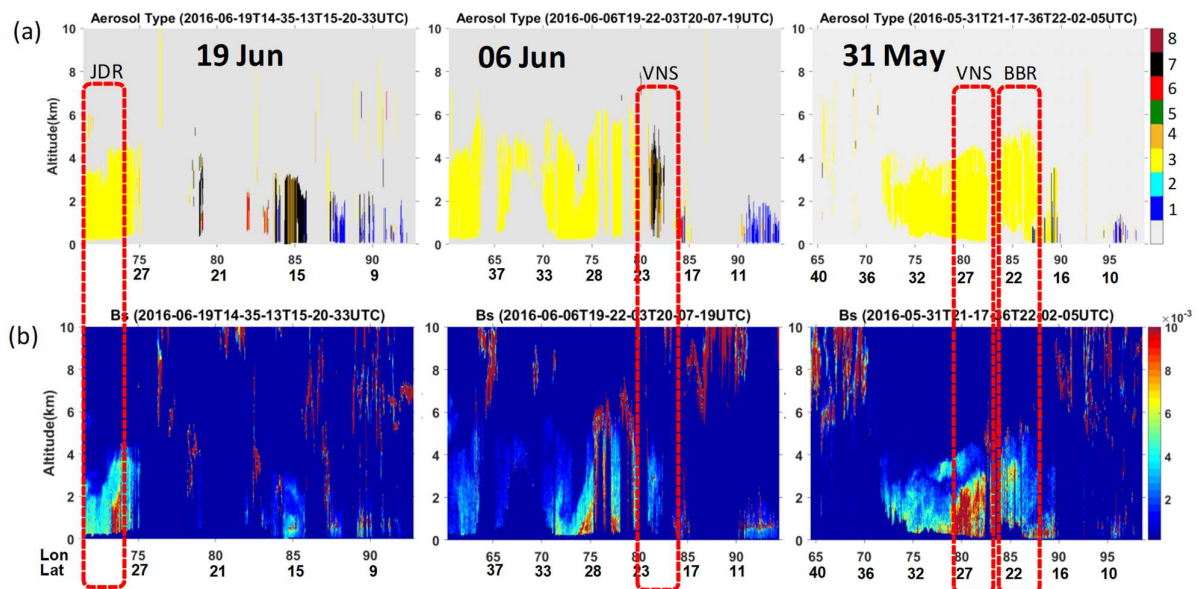
404



405

406 **Figure-9:** Aerosol Depolarization Ratio [obtained from Cloud Aerosol Transportation system in
 407 International Space Station (ISS)] for three different passes of the ISS over the three sub-regions
 408 during the period of aircraft observation. The tracks of the CATS are shown by the solid lines in the
 409 left panel and the rectangular boxes in the right panels show the data over the sub-regions.

410 Figure 9 shows the vertical cross-section of depolarization ratio for three passes during the campaign
 411 period and close to the three sub-regions (identified by the rectangular boxes in the figure). Higher
 412 values (~ 0.3) of depolarization ratios are seen in the western IGP (JDR, bottom panel), suggesting
 413 the dominance of non-spherical (dust) particles. The depolarization ratio decreases towards east
 414 across the IGP, with values equal to 0.1 at the central IGP, and ~ 0.2 in the eastern site BBR. These
 415 lend additional support to the inference on the influence of dust aerosols during the campaign period.
 416 Supporting the patterns of depolarization ratio, aerosol types (from CATS mode 7.1) in Figure 10a
 417 indicates significant presence of dust at JDR, while the aerosol types over VNS and BBR are mixture
 418 of dust, polluted continental and carbonaceous aerosols. Vertical profiles of total attenuated
 419 backscatter coefficients show the vertical extent of the aerosol layer to be as high as 5 km (as has
 420 been shown by Banerjee et al 2019) over all the sites (Figure 10b).



421

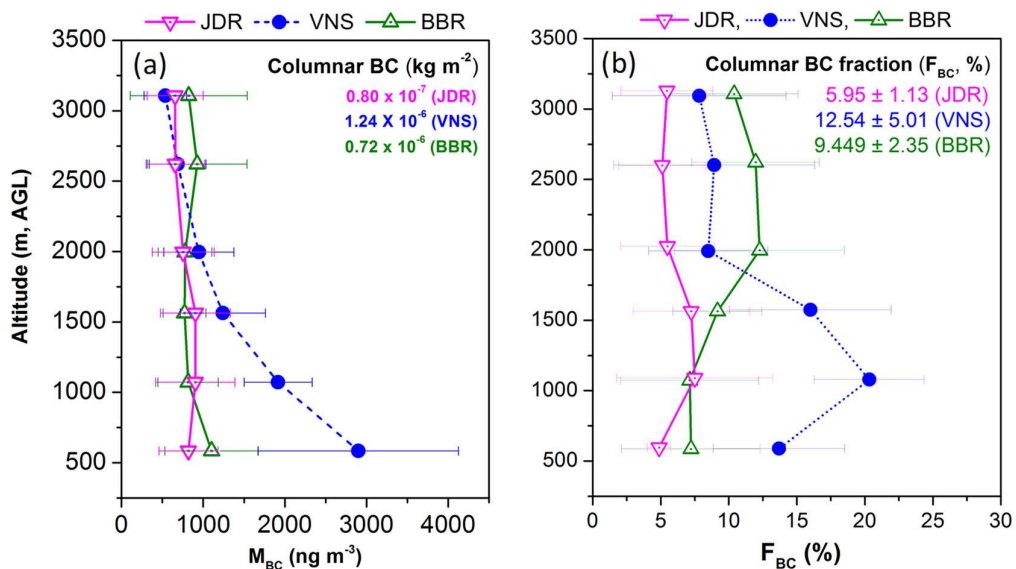
422 **Figure-10:** Transects of (a) Aerosol types (1- Marine, 2- Marine Mixture, 3- Dust, 4- Dust Mixture,
 423 5- Clean/ Background, 6- Polluted Continental, 7- Smoke, 8- Volcanic), and (b) Backscatter
 424 coefficients (B_s , $\text{km}^{-1}\text{Sr}^{-1}$) at 1064 nm obtained during the period of aircraft observation
 425 corresponding to the overpass of the ISS.

426

427 3.3 Vertical profiles of BC

428 BC is the chief anthropogenic absorbing aerosol species, and the IGP is known to be among the
 429 global hotspots (Govardhan et al., 2019). The height resolved information on F_{BC} is important not

430 only in radiative forcing, but on CCN activation as well (Bhattu et al., 2016). Collocated
 431 measurements of BC during SWAAMI - RAWEX have been used to examine the vertical profiles
 432 of BC and its variation across the IGP prior to onset of the Indian summer monsoon. Figure 11a
 433 shows the vertical profiles of BC for the three sub-regions. Each profile is the average of all the
 434 profiles obtained from measurements made from each of the base station. It is seen that, BC remained
 435 low ($\sim 1 \mu\text{g m}^{-3}$) and depicted very weak altitude variations at the western and eastern IGP regions,
 436 while in the central IGP there is a rapid decrease of BC from the high value ($\sim 3 \mu\text{g m}^{-3}$) near the
 437 surface. Above 2 km, all the profiles overlap though a weak increase is indicated over BBR, which
 438 is examined later. The very high values of BC close to the surface at VNS are attributed to the wide-
 439 spread anthropogenic activities in the Central IGP including the cluster of thermal power plants in
 440 that region. Consequently, the columnar concentration of BC (integrated up to 3.1 km) is also the
 441 highest at VNS.



442

443 **Figure-11:** Vertical profiles of (a) mean values of BC mass concentrations (M_{BC}) and (b) BC mass
 444 fractions (F_{BC}) at JDR, VNS and BBR.

445 However, the vertical profiles of the fractional contribution of BC (F_{BC}) to the total composite
 446 aerosol mass (estimated from the volume size distribution, considering a uniform density of 2 gm/cc ,
 447 especially in view of the abundance of dust) shows (Figure 11b) sub-regional distinctiveness. It
 448 remains the lowest ($\sim 6\%$) in the western IGP, with very little altitude variation. In the central IGP,
 449 F_{BC} is quite high ($\sim 15\%$ to 20%) within the ABL and drops off fast above 2 km approaching the
 450 values seen for the western IGP. F_{BC} depicts an elevated peak at around 1 km above ground level at
 451 VNS, while at BBR, higher F_{BC} values occur at still higher altitudes at BBR, where the near-surface

452 values are much lower and comparable to those at JDR. There is a steady increase in F_{BC} from near
453 surface to higher altitudes, and above 2 km, the values are comparable to the peak values seen at
454 VNS (at ~ 1 km altitude). Despite this, the integrated BC concentration comes in between those of
455 JDR and VNS, mainly because of the large values occurring in the lower atmosphere at VNS. It may
456 be recalled that based on SWAAMI - RAWEX aircraft measurements, Vaishya et al., (2018) have
457 reported that while the scattering characteristics remained uniform across the IGP, the absorption
458 coefficients showed sub-regional distinctiveness leading to a west to east gradient (decrease) in the
459 vertical structure of single scattering albedo (SSA).

460 Investigation of the vertical profiles of BC mass concentrations on individual days (Supplementary
461 Figure-S2) helps to see the distinctiveness at each sub-region, resulting from the spatially
462 heterogeneous nature of emission sources and advection, especially at BBR where the inland
463 profiles, made during sorties perpendicular to the coastline (on 2nd and 3rd June) show significantly
464 higher values of BC at higher altitudes than those along the coastline. At BBR, this arises mainly
465 because of spatially heterogeneous source impacts. The regions towards the northwest of BBR are
466 characterized by large scale urban and industrial activities (Ambient air quality status and trends in
467 Odisha: 2006 - 2014). Similarly, near surface BC concentrations at VNS was higher when the flight
468 sorties were confined to NE, NW and SW of the city Centre, while the values in the SE sector was
469 lower. On the other hand, at JDR, the profiles revealed a better spatial homogeneity.

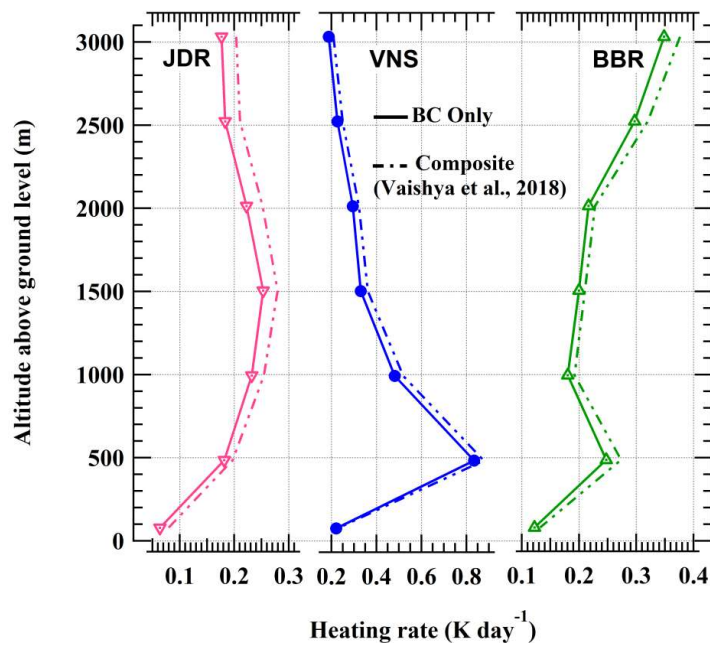
470 To quantify the climatic implications of BC, the heating rate profiles of BC is examined based on
471 the estimation of shortwave direct radiative forcing (DRF) due to BC alone. The DRF due to BC
472 represents the difference between the DRF for aerosols with and without the BC component. The in-
473 situ values of scattering (σ_{sca}) and absorption (σ_{abs}) coefficients measured on-board the aircraft were
474 used to estimate spectral values of AOD (layer-integrated $\sigma_{sca} + \sigma_{abs}$), single scattering albedo (SSA)
475 and asymmetry parameter (g) for each level, assuming a well-mixed layer of 200 m above and below
476 the measurement altitude (details are available in Vaishya et al., 2018). The layer mean values of
477 AOD, SSA and Legendre moments of the aerosol phase function (derived from Henyey–Greenstein
478 approximation) are used as input in the Santa Barbara DISORT Atmospheric Radiative Transfer
479 (SBDART, Ricchiazzi et al., 1998) model to estimate diurnally averaged DRF (net flux with and
480 without aerosols) at the top (DRF_{TOA}) and bottom (DRF_{SUR}) of each of the layers. The atmospheric
481 forcing (DRF_{ATM}) for each of the levels is then estimated as

$$482 \quad DRF_{ATM} = DRF_{TOA} - DRF_{SUR} \quad (3)$$

483 In order to estimate the forcing due to BC alone, optical parameters for aerosols were deduced again.
 484 For this, values of σ_{abs} were segregated to the contributions by BC (σ_{BC}) and OC (σ_{OC}), where σ_{BC}
 485 were estimated following inverse wavelength dependence of BC (e.g., Vaishya et al., 2017). Based
 486 on this, a new set of AOD and SSA for BC-free atmosphere is calculated and fed into SBDART for
 487 estimating $\text{DRF}_{\text{ALL-BC}}$ without the BC component. Thus, DRF due to BC is

$$488 \text{DRF}_{\text{BC}} = \text{DRF}_{\text{ALL}} - \text{DRF}_{\text{ALL-BC}} \quad (4)$$

489 Here, DRF_{ALL} represents forcing due to all the aerosol components, including BC.



490

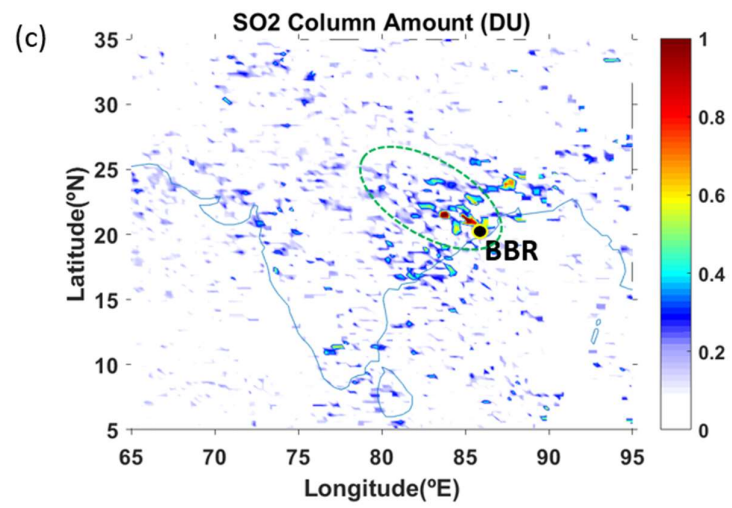
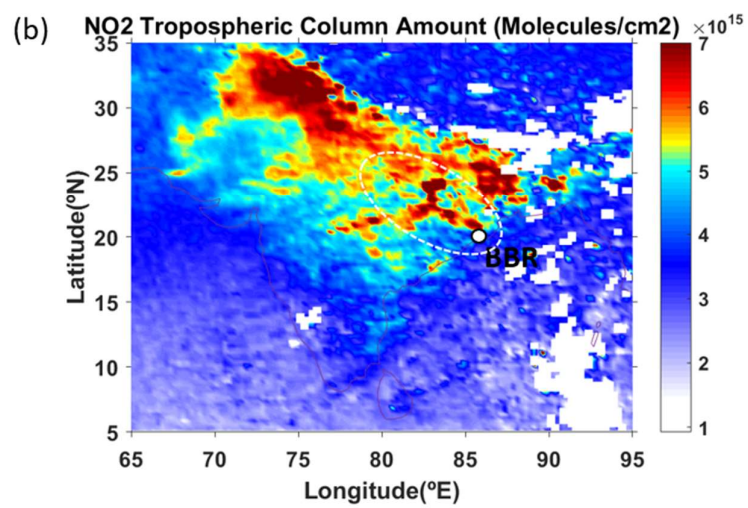
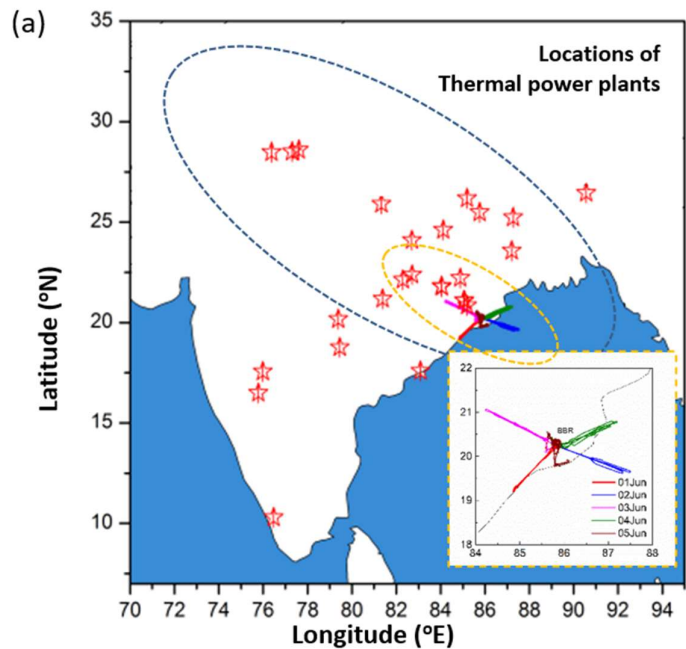
491 Figure-12: Vertical profiles of atmospheric heating rate due to BC (solid lines) and composite
 492 (dashed lines) aerosols for the regions of the IGP: (a) JDR in western IGP, (b) VNS in central IGP
 493 and (c) BBR in eastern IGP. Data for the composite heating rate profiles are from Vaishya et al.,
 494 2018.

495 The vertical profiles of atmospheric heating rate (HR, estimated based on the atmospheric pressure
 496 difference between top and bottom of each layer and aerosol induced forcing in that layer) due to
 497 BC alone shows (Figure-12) maximum influence of BC in trapping the SW-radiation at VNS,
 498 followed by BBR and JDR. Interestingly, the altitudinal profiles of heating rate are distinctly
 499 different over the regions, BBR showing an increase with altitude, while VNS shows the opposite
 500 pattern with maximum heating ($\sim 0.81 \text{ K day}^{-1}$) at 500 m above ground. Enhanced heating at 500-
 501 2000 m altitude is seen at JDR. These results indicate the dominant role of absorbing aerosols near

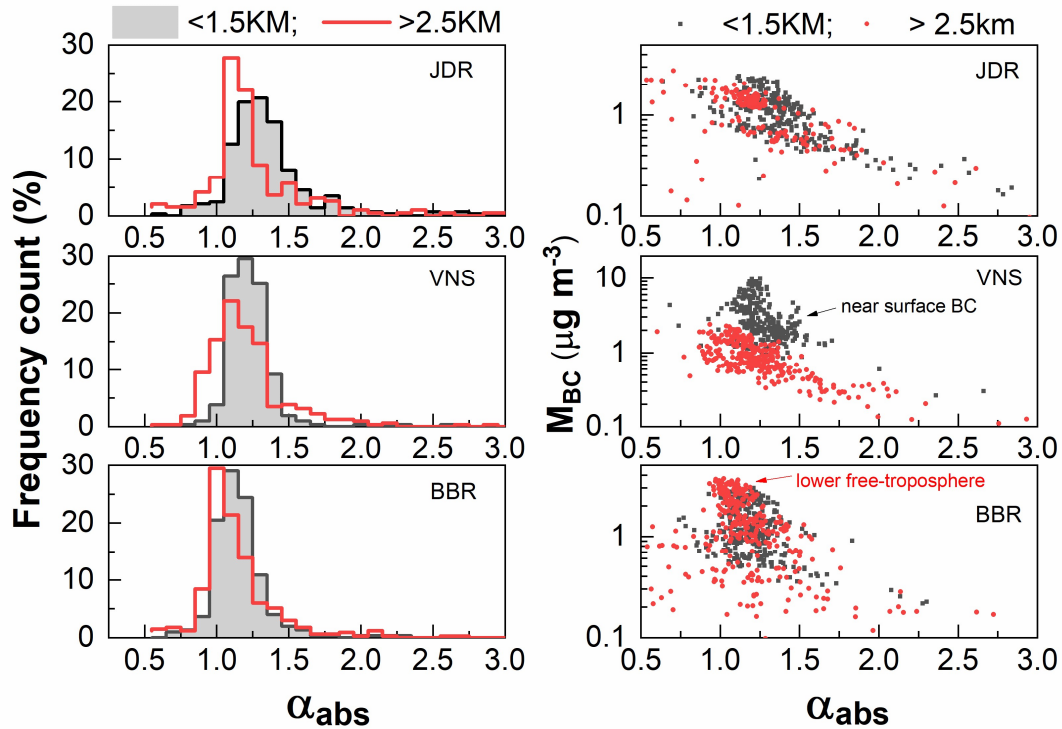
502 the surface at VNS, while the atmospheric perturbation due to elevated layers of absorbing aerosols
503 is conspicuous at BBR ($HR \sim 0.35 \text{ K day}^{-1}$ at the ceiling altitude). The column integrated values of
504 atmospheric forcing due to BC alone are 7.9 Wm^{-2} , 14.3 Wm^{-2} and 8.4 Wm^{-2} at JDR, VNS and BBR
505 respectively.

506 In this context, we have examined the possible role of the large network of thermal power plants
507 (TPP) over the northern part of India, which is reported to have a significant contribution to regional
508 emissions (Singh et al., 2018). These include the emissions of SO_2 , NO_x , CO_2 , CO, VOC, suspended
509 particulate matter (PM_{2.5} and PM₁₀, including BC and OC) and other trace metals like mercury
510 (Guttikanda and Jawahar, 2014; Sahu et al., 2017), dispersing over large areas through stacks. Fly
511 ash from coal-fired power plants cause severe environmental degradation in the nearby environments
512 (5-10 km) of TPP (Tiwari et al., 2019). Over the IGP, since more than 70% of the thermal power
513 plants are coal based, emissions of CO_2 and SO_2 hold more than 47% of the total emission share,
514 while the relative share of PM_{2.5} and NO_x are $\sim 15\%$ and 30% (GAINS, 2012). Based on the in-situ
515 measurement of BC in fixed and transit areas in close proximity of seven coal-fired TPP in Singrauli
516 (located $\sim 700 \text{ km}$ north-west of BBR), Singh et al., (2018) have reported that BC concentration
517 reached as high as $200 \mu\text{g m}^{-3}$ in the transit measurements. The Energy and Resources Institute,
518 India have also reported that emission levels of the carbonaceous (soot or BC) particles are estimated
519 to be around 0.061 gm/kWh per unit of electricity from Indian thermal power plants (Vipradas et al.,
520 2004). Based on emission pathways and ambient PM_{2.5} pollution over India, Venkataraman et al.,
521 (2018) have reported that the types of aerosols emitted from coal burning in thermal power plants
522 and industry in eastern and peninsular India are similar to that of residential biomass combustion.
523 The ongoing discussion thus clearly indicates that TPP are major sources of BC in the atmosphere.

524 As it is not possible to measure BC from space, to infer on the role of these emissions from thermal
525 power plants in causing the higher BC fraction at higher altitude over BBR, we have examined the
526 spatial distribution of the concentrations of the co-emitted NO_2 and SO_2 in Figure 13, in which the
527 locations of major coal based TPP (<https://www.ntpc.co.in/en/power-generation/coal-based-power-stations>)
528 are also marked. The data are obtained from OMI onboard AURA satellite. Higher
529 concentrations of NO_2 and SO_2 are readily discernible from the figure around the regions (marked
530 in the figure) during the period of flight experiment where there are clusters of TPP. As the energy
531 consumption is the highest during summer and most dependent on thermal, these TPP should be
532 operating to near full capacity. This provides an indirect support to the high concentrations of BC
533 (co-emitted) at higher levels. In general, these TPP have tall stacks (heights in the range 200 to 400
534 m) and aids easy ventilation to the lower free-tropospheric altitudes.



536 **Figure-13:** (a) Geographic position of thermal power plants (TPP) over India (the TPP across the
 537 IGP are bounded by the blue dashed line, and those along the flight direction of BBR are bounded
 538 by the green dashed line), along with the spatial map of (b) NO₂ tropospheric column density
 539 (molecules/cm²) and (c) SO₂ column amount (in DU, 1DU = 2.69 x 10¹⁶ molecules/cm²) over the
 540 northern part of India.



541
 542 **Figure-14:** (a) Frequency of occurrences of Angstrom absorption exponent (α_{abs}) below 1.5 km and
 543 above 2.5 km altitude, (b) variation of BC mass concentrations corresponding to different values of
 544 α_{abs} are shown in the right panels for the same two altitude regimes at distinct locations of northern
 545 India.

546 To further ascertain this, the spectral properties of aerosol absorption are examined. First, we have
 547 examined the frequency distribution of absorption Ångström exponent (α_{abs} , derived from the linear
 548 fit on log-log scale between corresponding absorption coefficients to aethalometer wavelengths) in
 549 Figure 14; separately for the mixed layer (ML, below 1.5 km) and above (≥ 2 km). The frequency
 550 distribution of α_{abs} reveals a clear shift towards lower values as we move from JDR to BBR, both
 551 within the ML and above, even though the values of α_{abs} lying mostly between 1 and 1.5. Based on
 552 laboratory studies and field investigations, it has been shown that the higher values of α_{abs} (~ 2) are
 553 representative of biomass burning emissions, while the values ~ 1 are indicative of fossil fuel
 554 combustions (Kirchstetter et al., 2004). The values of $\alpha_{abs} > 1$ is indicative of the presence of biomass-

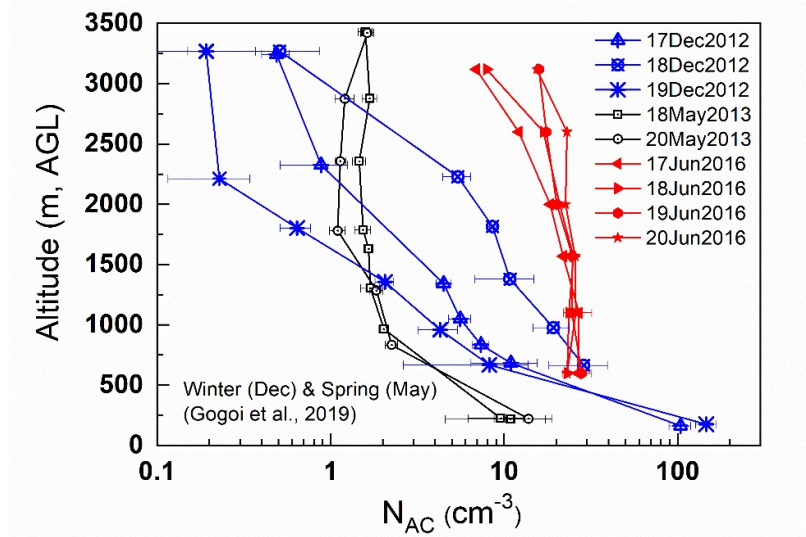
555 burning, whose relative abundance increase with the steepness of the absorption spectra, as has been
556 reported elsewhere from the laboratory experiments (Hopkins et al., 2007).

557 Examining Figure 14 in the above light, it emerges that significant contribution of BC from fossil
558 fuel combustions mixed with biomass burning origin prevails at higher altitudes over BBR, while
559 the association between the two decreases abruptly from ML to higher height at VNS. The consistent
560 higher values of BC in the column associated with the values of α_{abs} lying between 1 and 1.5 can
561 also be due to the aging of BC at higher heights, during which BC mixes with other species and its
562 angstrom exponent increases, as the spectral dependence of absorption steepens when BC (even
563 though its source could be fossil fuel) is coated with a concentric shell of weakly absorbing material
564 (Gogoi et al., 2017). Further investigations are needed in this direction.

565 3.4 Inter-seasonal variability: a case study at JDR

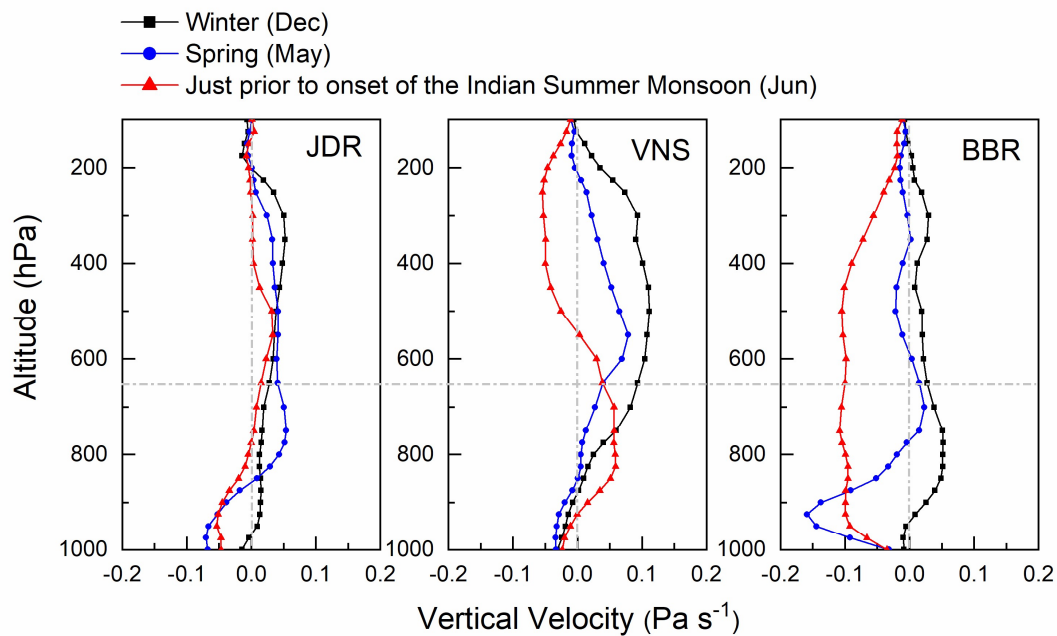
566 The spatial variation of the altitude profiles of N_{AC} , D_g , F_{MC} and F_{BC} across the IGP hints to several
567 possible implications of their direct and indirect effects. Altitudinal increases in the values of D_g
568 and F_{MC} along with depolarization ratios are indicative of the presence of dust ($> 4 \mu\text{m}$) in the lower
569 free troposphere, which is known to produce long-wave (warming) radiative effect (Miller et al.,
570 2006; Tegen and Lacis, 1996). Conversely, significant abundance of accumulation mode aerosols,
571 in general, might contribute significantly to scattering. For example, a clear seasonal change in the
572 vertical profiles of N_{AC} is noticeable at JDR, changing of the much steeper variation (vertically) in
573 winter (as reported by Gogoi et al., 2019) to a near-steady one during just prior to the onset of
574 monsoon (Figure 15). Based on air-borne measurements during SWAAMI - RAWEX, Vaishya et
575 al., (2018) have reported that the values of SSA at west IGP varied between 0.935 (at 530) in spring
576 to 0.84 (at 530 nm) during prior to onset of monsoon, indicating a seasonal change in the aerosol
577 type and consequently their optical properties.

578 To examine the role of the dynamical processes at different seasons, we have shown the profiles of
579 vertical velocity (in pressure coordinates from 1000 hPa to 100 hPa) in Figure 16. These are obtained
580 from ERA-interim reanalysis data sets. Here, the positive and negative signs of vertical velocity (ω)
581 are indicative of updraft (as indicated by -ve values of ω) and downdraft (as indicated by +ve values
582 of ω). A clear seasonal transformation is seen, with increasingly stronger updrafts dominating over
583 the IGP from December to June, with the intensity increasing from west to east. In the western IGP
584 regions, the sign of vertical velocity is seemed to change from December to June, progressively
585 enhancing the magnitude of deep convection towards the onset of monsoon imparting stronger
586 vertical dispersion and more homogeneous distribution of aerosols in the column.



587

588 **Figure-15:** Vertical profiles of seasonal mean values of aerosol accumulation and coarse mode
 589 number concentrations (N_{AC}) at Jodhpur during winter-2012 (17-19 Dec), spring-2013 (18 and 20
 590 May) and just prior to the onset of monsoon-2016 (17-20 June).



591

592 **Figure-16:** Vertical profiles of vertical velocity (Pa s^{-1}) over the study locations representing Winter
 593 (December, 2012), Spring (May, 2013) and just prior to onset of the Indian Summer Monsoon (June,
 594 2016) at different pressure levels from 1000 to 100 hPa. The positive and negative values are
 595 indicative of the descending and ascending motions respectively. The horizontal dashed line
 596 indicated the ceiling altitude (~ 3.5 km above ground level) of aircraft measurements while the

597 vertical dashed lines mark the boundary of vertical velocity ($= 0$) changing from positive to negative
598 and vice versa.

599 Regionally, the seasonal transformation of vertical velocity is more prominent over the eastern IGP
600 -'BBR', where the magnitude of vertical velocity is consistently higher from surface to upper
601 tropospheric regions prior to the onset of monsoon. During this period, the head-Bay of Bengal is
602 known to be one of the regions where deep convection exists (Bhat et al., 2001). Since size
603 distribution is a dominant factor in determining the direct radiative forcing (Tegen and Lacis, 1996;
604 Liao and Seinfeld, 1998; Seinfeld et al., 2016), a clear seasonal change in the altitudinal variations
605 of aerosol type and size distributions associated with distinct transport and convective processes will
606 have strong radiative impact. Especially the columnar distribution of coarse mode dust and highly
607 absorbing BC need explicit representations in climate models for accurate understanding of the net
608 TOA direct radiative forcing. Apart from the direct radiative implications, abundance of coarse mode
609 dust particles (having sizes larger than critical diameter) and aged BC (coated with hygroscopic
610 materials) in the lower free troposphere can act as cloud condensation nuclei (CCN) in a
611 supersaturated environment. Recent studies suggest that mineral aerosols are the dominant ice nuclei
612 for cirrus clouds (Storelvmo and Herger, 2014).

613 **4. Summary and Conclusions**

614 Extensive air-borne measurements of aerosol number-size distribution profiles are carried out, for
615 the first time across the IGP prior to the onset of Indian summer monsoon as part of SWAAMI -
616 RAWEX. Collocated measurements of BC profiles are also carried out. The main findings are:

- 617 • Aerosol size distribution depicted significant altitudinal variation in the coarse mode regime,
618 at western IGP (represented by JDR), having highest coarse mode mass fraction (72%) near
619 the surface; while BC mass fractions (F_{BC}) as well as aerosol accumulation and coarse mode
620 number concentrations (N_{AC}) remained nearly steady from surface to the ceiling altitude (\sim
621 3.5 km) of the aircraft measurements. However, the pattern was significantly different at
622 eastern IGP (represented by BBR) transforming to gradually decreasing values of coarse
623 mode mass concentration (M_C) and N_{AC} , but with a corresponding increase in the values of
624 F_{BC} with altitude. At sub-regional scales, BBR depicted higher spatial heterogeneity in the
625 above aerosol characteristics; while highest homogeneity was observed at JDR.

- 626 • Number concentrations showed dominance of accumulation mode near the surface, with the
627 Central IGP station Varanasi (VNS) depicting the highest values N_{AC} ($F_{BC} \sim 15\%$), while the
628 coarse mode remained nearly steady throughout the vertical column.
- 629 • Atmospheric heating rate due to BC is highest near the surface at VNS ($\sim 0.81 \text{ K day}^{-1}$),
630 while showing an increasing pattern with altitude at BBR ($\sim 0.35 \text{ K day}^{-1}$) at the ceiling
631 altitude.
- 632 • Our measurements, supplemented with information from different space-borne sensors
633 (CATS aboard ISS; OMI) and model results clearly indicated role of mineral dust; both
634 locally generated and advected from the west Asian region, in contributing to the aerosol
635 loading across the IGP, especially at free-tropospheric altitudes. The vertical extents of these
636 layers reached as high as 5 km during the period of observation.

637

638 **Data availability**

639 Details of aircraft data used in this manuscript and the point of contact are available at
640 <http://spl.gov.in>; “Research Themes”; “Aerosols and Radiative Forcing”.

641 **Authors contributions**

642 SSB, SKS and KKM conceptualized the experiment and finalized the methodology. SSB, MMG, VJ
643 and AV conducted the measurement on board aircraft. MMG carried out the scientific analysis of
644 the aircraft data and drafted the manuscript with contributions from AV and VJ. KKM, SKS and
645 SSB carried out the review and editing of the manuscript.

646 **Competing interests**

647 The authors declare that they have no conflict of interest.

648 **Acknowledgement**

649 This study was a part of joint Indo-UK field campaign, South-West Asian Aerosol Monsoon
650 Interactions - Regional Aerosol Warming Experiment (SWAAMI - RAWEX). The aircraft and the
651 flying support were provided by National Remote Sensing Centre (NRSC), Hyderabad. SKS would
652 like to acknowledge J.C. Bose Fellowship awarded to him by SERB-DST. AV was supported by the
653 Department of Science and Technology, Government of India through its INSPIRE Faculty
654 programme. We acknowledge the CATS science team for providing valuable data sets (freely) for
655 scientific applications. The RAWEX project is supported by ISRO (Indian Space Research

656 Organisation) and the SWAAMI project is supported by MoES (Ministry of Earth Science),
657 Government of India.

658

659 **References**

660 Ambient air quality status and trends in Odisha: 2006 – 2014: Published by State Pollution Control
661 Board, Odisha, 2015.

662 Arnott, W. P., Hamasha, K., Moosmuller, H., Sheridan, P.J. and Ohren, J.A.: Towards aerosol light-
663 absorption measurements with a 7-wavelength aethalometer: Evaluation with a photoacoustic
664 instrument and 3-wavelength nephelometer. *Aerosols Sci. Technol.*, 39(1), 17-29, 2005.

665 Babu, S.S., Nair, V.S., Gogoi, M.M. and Moorthy, K.K.: Seasonal variation of vertical distribution
666 of aerosol single scattering albedo over Indian sub-continent: RAWEX aircraft observations.
667 *Atmos. Environ.*, 125, 312–323, <https://doi.org/10.1016/j.atmosenv.2015.09.041>, 2016.

668 Banerjee, P., Satheesh, S.K., Moorthy, K.K., Nanjudiah, R.S., Nair, V.S.: Long-Range Transport of
669 Mineral Dust to the Northeast Indian Ocean: Regional versus Remote Sources and the
670 Implications, *J. Climate*, 32, 1525-1549, DOI: 10.1175/JCLI-D-18-0403.1, 2019.

671 Bansal, O., Singh, A., Singh, D.: Aerosol Characteristics over the Northwestern Indo-Gangetic Plain:
672 Clear-Sky Radiative Forcing of Composite and Black Carbon Aerosol, *Aerosol Air Quality*
673 *Res.*, 19: 5–14, 2019.

674 Bhat, G.S., Gadgil, S., Kumar, P.V.S., Kalsi, S.R., Madhusoodanan, P., Murty, V.S.N., Rao,
675 V.V.K.P., Babu, V.R., Rao, L.V.G., Rao, R.R., Ravichandran, R., Reddy, K.G., Rao, P.S.,
676 Sengupta, D., Sikka, D.R., Swain, J. and Vinayachandran, P.N.: BOBMEX: The Bay of Bengal
677 Monsoon Experiment, *Bull. American Met. Society*. 82, 10, 2217-2243, 2001.

678 Bhattu, D., Tripathi, S., Chakraborty, A.: Deriving aerosol hygroscopic mixing state from size-
679 resolved ccn activity and HR-TOF-AMS measurements, *Atmos. Environ.*, 142, 57-70, 2016.

680 Brooks, J., James D.A., Paul I. et al.: Vertical and horizontal distribution of submicron aerosol
681 chemical composition and physical characteristics across northern India during pre-monsoon
682 and monsoon seasons. *Atmos. Chem. Phys.* 19, 5615–5634, 2019.

683 Corrigan, C.E., Ramanathan, V. and Schauer, J.J.: Impact of monsoon transitions on the physical
684 and optical properties of aerosols. *J. Geophys. Res.*, 111, D18208,
685 [doi:10.1029/2005JD006370](https://doi.org/10.1029/2005JD006370), 2006.

686 Gautam, R., Hsu, N.C. and Lau, K.M.: Premonsoon aerosol characterization and radiative effects
687 over the Indo-Gangetic Plains: Implications for regional climate warming, *J. Geophys. Res.*,
688 115, D17208, doi:10.1029/2010JD013819, 2010.

689 Gautam, R., Hsu, N.C., Tsay, S.C., Lau, K.M., Holben, B., Bell, S. et al.: Accumulation of aerosols
690 over the Indo-Gangetic plains and southern slopes of the Himalayas: distribution, properties
691 and radiative effects during the 2009 pre-monsoon season. *Atmos. Chem. Phys.* 11, 12841–
692 12863, 2011.

693 Giles, D. M., Holben, B. N., Eck, T. F., Sinyuk, A., Smirnov, A., Slutsker, I., Dickerson, R. R.,
694 Thompson, A. M. and Schafer, J. S.: An analysis of AERONET aerosol absorption properties
695 and classifications representative of aerosol source regions, *J. Geophys. Res.*, 117, D17203,
696 doi:10.1029/2012JD018127, 2012.

697 Gogoi, M.M., Babu, S.S., Moorthy, K.K., Bhuyan, P.K., Pathak, B., Subba, T., Chutia, L., Kundu,
698 S.S., Bharali, C., Borgohain, A., Guha, A., De, B.K., Singh, B., and Chin, M.: Radiative effects
699 of absorbing aerosols over northeastern India: Observations and model simulations. *J.*
700 *Geophys. Res.*, 122, doi:10.1002/2016JD025592, 2017.

701 Gogoi, M.M., Lakshmi, N.B., Nair, V.S., Kompalli, S.K., Moorthy, K.K. and Babu, S.S., 2019.
702 Seasonal contrast in the vertical profiles of aerosol number concentrations and size
703 distributions over India: implications from RAWEX aircraft campaign. *J. Earth Sys. Sc.*, 128
704 225, DOI: 10.1007/s12040-019-1246-y, 2019.

705 Govardhan, G., Satheesh, S.K., Moorthy, K.K. and Nanjundiah, R.: Simulations of Black Carbon
706 Over Indian Region: Improvements and implications of diurnality in emissions *Atmos. Chem.*
707 *Phys.*, 19, 8229–8241, <https://doi.org/10.5194/acp-19-8229-2019>, 2019.

708 Jayachandran, V.N., Babu, S.S., Vaishya, V., Gogoi, M.M., Nair, V.S., Satheesh, S.K., Moorthy,
709 K.K.: Altitude profiles of cloud condensation nuclei characteristics across the Indo-Gangetic
710 Plain prior to the onset of the Indian summer monsoon, *Atmos. Chem. Phys.*, 20, 561–576,
711 doi:10.5194/acp-20-561-2020, 2020

712 Kedia, S., Ramachandran, S., Holben, B.N., Tripathi, S.N.: Quantification of aerosol type, and
713 sources of aerosols over the Indo-Gangetic Plain. *Atmos. Env.*, 98, 607-619, 2014.

714 Kirchstetter, T. W., Novakov, T. and Hobbs, P. V.: Evidence that the spectral dependence of light
715 absorption by aerosols is affected by organic carbon, *J. Geophys. Res.*, 109, D21208,
716 doi:10.1029/2004JD004999, 2004.

717 Kulkarni, J. R., Maheskumar, R. S., Morwal S. B; Padma Kumari B., Konwar M., Deshpande C. G.,
718 Joshi R. R., Bhalwankar R. V., Pandithurai G., Safai P.D., Narkhedkar S. G., Dani K. K., Nath
719 A., Nair Sathy, Sapre V. V., Puranik P. V., Kandalgaonkar S., Mujumdar V. R., Khaladkar R.
720 M., Vijayakumar R., Prabha T. V. and Goswami B. N.: The Cloud Aerosol Interactions and
721 Precipitation Enhancement Experiment (CAIPEEX): Overview and Preliminary Results,
722 *Current Science*, 102(3), 413-425, 2012.

723 Kumar, M., Parmar, K.S., Kumar, D.B., Mhawish, A., Broday, D.M., Malla, R.K., Banerjee, T.:
724 Long-term aerosol climatology over Indo-Gangetic Plain: Trend, prediction and potential
725 source fields. *Atmos. Env.*, 180, 37–50, 2018.

726 Lee et al.: Investigation of CATS aerosol products and application toward global diurnal variation
727 of aerosols, *Atmos. Chem. Phys. Discuss.*, <https://doi.org/10.5194/acp-2018-1298> 2019.

728 Levelt, P. F., van den Oord, G. H. J., Dobber, M. R., Mälkki, A., Visser, H., de Vries, J., Stammes,
729 P., Lundell, J. O. V., and Saari, H.: The Ozone Monitoring Instrument, *IEEE Trans. Geosci.
730 Remote Sens.*, 44, 1093–1101, doi:10.1109/TGRS.2006.872333, 2006.

731 Li, Z., et al.: Aerosol and monsoon climate interactions over Asia, *Aerosol and monsoon climate
732 interactions over Asia*, *Rev. Geophys.*, 54, 866–929, doi:10.1002/2015RG000500, 2016.

733 Liao, H. and Seinfeld, J.H.: Radiative forcing by mineral dust aerosols: Sensitivity to key variables.
734 *J. Geophys. Res.*, 103, 31,637–31, 645, 1998.

735 Mhawish, A., Banerjee, T., Broday, D.M., Misra, A., Tripathi, S.N.: Evaluation of MODIS
736 Collection 6 aerosol retrieval algorithms over IndoGangetic Plain: Implications of aerosols
737 types and mass loading, *Remote Sens. Env.*, 201, 297–313, 2017.

738 Miller, R. L. et al.: Mineral dust aerosols in the NASA Goddard Institute for Space Sciences ModelE
739 atmospheric general circulation model. *J. Geophys. Res.* 111, D06208,
740 doi:10.1029/2005JD005796, 2006.

741 Mitchell, J.P. and Nagel, M.W., Time-of-flight aerodynamic particle size analysers: their use and
742 limitations for the evaluation of medical aerosols, *J. Aerosol. Medicine*, 12, 4, 217-240,
743 1999.

744 Moorthy, K. K., Babu, S.S., Satheesh, S.K., Srinivasan, J. and Dutt, C.B.S.: Dust absorption over
745 the “Great Indian Desert” inferred using ground-based and satellite remote sensing, *J.
746 Geophys. Res.*, 112, D09206, doi:10.1029/2006JD007690, 2007.

747 Moorthy, K.K., Babu, S.S., Satheesh, S.K., Srinivasan, J. and Dutt, C.B.S.: Dust absorption over the
748 “Great Indian Desert” inferred using ground-based and satellite remote sensing. *J. Geophys.*
749 *Res.*, 112, D09206, doi:10.1029/2006JD007690, 2007.

750 Moorthy, K.K., Satheesh, S.K. and Kotamarthi, V.R., Evolution of aerosol research in India and
751 the RAWEX–GVAX: an overview, *Current Sc.*, 111, 1, 2016.

752 Moorthy, K.K., Satheesh, S.K., Murthy, B.V.K.: Characteristics of spectral optical depths and size
753 distributions of aerosols over tropical oceanic regions, *J. Atmos. Sol. Terr. Phys.*, 60, 981-992,
754 1998.

755 Nair, V. S., Babu, S.S., Gogoi, M.M. and Moorthy, K.K.: Large-scale enhancement in aerosol
756 absorption in the lower free troposphere over continental India during spring, *Geophys. Res.*
757 *Let.*, 43, 11,453–11,461, doi:10.1002/2016GL070669, 2016.

758 Nath, R., Luo, Y., Chen, W. and Cui, X.: On the contribution of internal variability and external
759 forcing factors to the Cooling trend over the Humid Subtropical Indo-Gangetic Plain in India.
760 *Sci. Reports.*, 8:18047, DOI:10.1038/s41598-018-36311-5, 2018.

761 Padmakumari, B., Maheskumar, R.S., Harikishan, G., Morwal, S.B., Prabha, T.V., Kulkarni, J.R.:
762 In situ measurements of aerosol vertical and spatial distributions over continental India during
763 the major drought year 2009, *Atmos. Env.*, 80, 107-121, 2013.

764 Panda, U., Das, T.: Micro-structural analysis of individual aerosol coarse particles during different
765 seasons at an eastern coastal site in India. *Atmos. Pollution Res.*, DOI:
766 10.1016/j.apr.2016.08.012, 2016.

767 Pandey, S.K., Vinoj, V., Landu, K. and Babu, S.S.: Declining pre-monsoon dust loading over South
768 Asia: Signature of a changing regional climate. *Sci. Reports.*, 7:16062, DOI:10.1038/s41598-
769 017-16338-w, 2017.

770 Pillai, P. S., and Moorthy, K.K.: Aerosol mass-size distributions at a tropical coastal environment:
771 Response to mesoscale and synoptic processes, *Atmos. Environ.*, 35, 4099– 4112, 2001.

772 Praveen, P.S., Ahmed, T., Kar, A., Rehman, I.H. and Ramanathan, V.: Link between local scale BC
773 emissions in the Indo-Gangetic Plains and large scale atmospheric solar absorption, *Atmos.*
774 *Chem. Phys.*, 12, 1173–1187, 2012.

775 Rana, A., Jia, S., Sarkar, S.: Black carbon aerosol in India: A comprehensive review of current status
776 and future prospects. *Atmos. Res.*, 218, 207–230, 2019.

777 Seinfeld, J.H. et al., 2016. Improving our fundamental understanding of the role of aerosol-cloud
778 interactions in the climate system. *Proc. Natl. Acad. Sci. U S A.* 113(21): 5781–5790.

779 Singh, A., Khadak S.M., Ruphakeri, M., Junkermann, W., Panday, A.K., Lawrence, M.G.: An
780 overview on the airborne measurement in Nepal, part 1: vertical profile of aerosol size-number,
781 spectral absorption and meteorology. *Atmos. Chem. Phys. Discuss.*
782 <https://doi.org/10.5194/acp-2018-95>, 2018.

783 Srivastava, R.: Trends in aerosol optical properties over South Asia, *Int. J. Climatol.*, 37, 1, 371-
784 380, DOI: 10.1002/joc.4710, 2016.

785 Storelvmo, T. and Herger, N.: Cirrus cloud susceptibility to the injection of ice nuclei in the upper
786 troposphere. *J. Geophys. Res.* 119, doi:10.1002/2013JD020816, 2014.

787 Tegen, I. and Lacis, A. A.: Modelling of particle size distribution and its influence on the radiative
788 properties of mineral dust aerosol, *J. Geophys. Res.*, 101, 19, 237–19,244 1996.

789 Vadrevu, K.P., Ellicott, E., Badarinath, K.V.S., Vermote, E.: MODIS derived fire characteristics and
790 aerosol optical depth variations during the agricultural residue burning season, north India,
791 *Env. Pollution*, 159, 1560-1569, 2011.

792 Vaishya, A., Babu, S.S., Jayachandran, V., Gogoi, M.M., Lakshmi, N.B., Moorthy, K.K. and
793 Sathesh, S.K.: Large contrast in the vertical distribution of aerosol optical properties and
794 radiative effects across the Indo-Gangetic Plain during the SWAAMI–RAWEX campaign.
795 *Atmos. Chem. Phys.*, 18, 17669–17685, 2018.

796 Venkataraman, C., Habib, G., Kadamba, D., Shrivastava, M., Leon, J.F., Crouzille, B., Boucher, O.
797 and Streets, D.G.: Emissions from open biomass burning in India: Integrating the inventory
798 approach with high-resolution Moderate Resolution Imaging Spectroradiometer (MODIS)
799 active-fire and land cover data, *Global Biogeochem. Cycles*, 20, GB2013,
800 doi:10.1029/2005GB002547, 2006.

801 Weingartner, E., Saathoff, H., Schnaiter, M., Streit, N., Bitnar, B. and Baltensperger, U.: Absorption
802 of light by soot particles: Determination of the absorption coefficient by means of
803 aethalometers. *J. Aerosol Sci.* 34, 1445– 1463, 2003.

804 Yorks, J. E.: An overview of the CATS level 1 processing algorithms and data products, *Geophys.*
805 *Res. Lett.*, 43, 4632–4639, doi:10.1002/2016GL068006, 2016.

806 Yorks, J. E.: The Airborne Cloud–Aerosol Transport System: Overview and Description of the
807 Instrument and Retrieval Algorithms, *J. Atmos. Oceanic Tech.*, 31, 2482-2497, doi:
808 10.1175/JTECH-D-14-00044.1, 2014.

809 Banerjee, P., Satheesh, S.K., Moorthy, K.K., Nanjundiah, R.S., Nair, V.S.: Long-range transport of
810 mineral dust to the Northeast Indian Ocean: regional versus remote sources and the
811 implications, *J. Climate*, 32, 1525-1549, doi: 10.1175/JCLI-D-18-0403.1, 2019.

812 GAINS, Greenhouse Gas and Air Pollution Interactions and Synergies - South Asia Program.
813 International Institute of Applied Systems Analysis, Laxenburg, Austria, 2010.

814 Guttikunda, S.K. and Jawahar, P.: Atmospheric emissions and pollution from the coal-fired thermal
815 power plants in India, *Atmos. Env.* 92, 449-460
816 <http://dx.doi.org/10.1016/j.atmosenv.2014.04.057>, 2014.

817 Hopkins, R. J., Tivanski, A.V., Marten, B.D., and Gilles, M. K., Chemical bonding and structure of
818 black carbon reference materials and individual carbonaceous atmospheric aerosols, *J. Aerosol*
819 *Sci.* 38, 573–591, 2007.

820 Moorthy, K. K., Babu, S.S., Sunilkumar, S.V., Gupta, P.K., and Gera, B.S.: Altitude profiles of
821 aerosol BC, derived from aircraft measurements over an inland urban location in India,
822 *Geophys. Res. Lett.* 31, L22103, doi:10.1029/2004GL021336, 2004.

823 Ricchiazzi, P., Yang, S., Gautier, C., and Sowle, D.: SBDART: A research and teaching software
824 tool for plane-parallel radiative transfer in the Earth’s atmosphere, *B. Am. Meteor. Soc.*, 79,
825 2101–2114, 1998.

826 Sahu, S.K., Ohara, T., and Beig, G.: The role of coal technology in redefining India’s climate change
827 agents and other pollutants *Environ. Res. Lett.* 12, 105006, [https://doi.org/10.1088/1748-](https://doi.org/10.1088/1748-9326/aa814a)
828 [9326/aa814a](https://doi.org/10.1088/1748-9326/aa814a), 2017.

829 Drinovec, L., Mocnik, G., Zotter, P., Prévôt, A.S.H., Ruckstuhl, C., Coz, E., Rupakheti, M., Sciare,
830 J., Müller, T., Wiedensohler, A., Hansen, A.D.A.: The “dual-spot” Aethalometer: an improved
831 measurement of aerosol black carbon with real-time loading compensation, *Atmos.*
832 *Measurement Tech.*, 8, 1965-1979, 2015.

833 Tiwari, M.K., Bajpai, S., Dewangan. U.K., Environmental Issues in Thermal Power Plants – Review
834 in Chhattisgarh Context, *J. Mater. Environ. Sci.* 10(11), 1123-1134, 2019.

835 Vaishya, A., Singh, P., Rastogi, S., and Babu, S. S.: Aerosol black carbon quantification in the
836 central Indo-Gangetic Plain: Seasonal heterogeneity and source apportionment, *Atmos. Res.*,
837 185, 13–21, <https://doi.org/10.1016/j.atmosres.2016.10.001>, 2017.

838 Venkataraman., C., Brauer, M., Tibrewal, K., Sadavarte, P., Ma, Q., Cohen, A., Chaliyakunne, S.,
839 Frostad, J., Klimont, Z., Martin, R.V., Millet, D.B., Philip, S., Walker, K., and Wang, S.:
840 Source influence on emission pathways and ambient PM_{2.5} pollution over India (2015–2050),
841 *Atmos. Chem. Phys.*, 18, 8017–8039, <https://doi.org/10.5194/acp-18-8017-2018>, 2018

842 Vipradas, M., Babu, Y.D., Garud, S., and Kumar, A., Preparation of road map for mainstreaming
843 wind energy in India, TERI project report No. 2002RT66, The Energy and Resources Institute,
844 2014.

845

846

847
